Supporting Information

Flexibility Coexists with Shape-persistence in Cyanostar Macrocycles

Yun Liu,[†] Abhishek Singharoy,[†] Christopher G. Mayne,[†] Arkajyoti Sengupta,
Krishnan Raghavachari,* Klaus Schulten,* Amar H. Flood*

[†]These authors contributed equally to this work.
*Emails of corresponding authors: kraghava@indiana.edu, schulten@illinois.edu, aflood@indiana.edu

Supplementary Documents

(1) Cyanostar Conformations.mol & Cyanostar Transition States.mol;
(2) Movie S1.mpg & Movie S2.mpg

Instructions. The 34 geometries in Cyanostar Conformations.mol file and 9 in Cyanostar Transition States.mol file can be opened as text files. Coordinates can either be extracted or visualized in Spartan (see Spreadsheet function under Display) and Mercury (see "structure" in the structure navigator). Two movies are attached for better visualization of the 34 conformations.

S.1   Conformational Landscape of a Single Cyanostar: DFT Calculation

The initial geometries were obtained either by exploiting combinations of cyano group orientations or MD simulations. These geometries were then optimized by DFT computations using the Gaussian suite of programs[S1] and the M06-2X functional.[S2] Cyanostars were modeled with hydrogen atoms in place of the *t*-butyl groups. The optimization was performed using the 6-31+g(d,p) basis set with implicit solvation of CH_2Cl_2 (IEFPCM model).[S3] Vibrational frequencies, zero point corrections and thermal corrections were conducted with the same basis set to verify the stationary points to be minimum energy structures (Figure S1). In particular, Grimme's quasi-RRHO approach[S4] was applied to the entropy contributions of low-lying vibrational frequencies ($\nu < 200$ cm^{-1}), whose appearance has been minimized by using very tight optimization convergence criteria with ultrafine integration grids specified. The parameters used in Grimme's method include: the cut-off frequency, $\nu_0 = 100$ cm^{-1}; the Head-Gordon damping factor, $\alpha = 4$; the average molecular moment of inertia, $B_{av} \sim 10^{-44}$ kg m^{-2}, which were calculated from corresponding rotational entropies. Single-point energy calculations with implicit solvation of CH_2Cl_2 using the IEFPCM model were carried out subsequently for the optimized geometries at the higher M06-2X/6-311++g(3df,2p) level of theory. The results are summarized in Tables S1 and S2, and coordinates in the appended *Cyanostar Conformations.mol*.

Table S1. DFT characterizations on conformers for a single cyanostar.

Isomers^a	E_{solv} (Hartree)^b	G_{corr} (Hartree)^c	TS_{corr}(Vib) (Hartree)^d	ΔG_{soln} (kcal/mol)^e	p_{soln} (%)^f
P_5	−2003.351372	0.493076	−0.010138	2.6	0.4
M_1P_4	−2003.352709	0.492574	−0.010307	0.6	12.9
M_1P_4-1	−2003.350452	0.492827	−0.010089	2.0	1.1
M_1P_4-2	−2003.350063	0.493270	−0.009897	2.4	0.6
M_1P_4-3	−2003.348631	0.492466	−0.010312	3.0	0.2
M_1P_4-4	−2003.347382	0.492603	−0.010156	3.8	0.05
M_1P_4-5	−2003.349130	0.493356	−0.009843	3.0	0.2
M_1P_4-1,3	−2003.350018	0.492346	−0.010515	2.2	0.8
M_1P_4-1,4	−2003.348872	0.492867	−0.010145	3.0	0.2
M_1P_4-2,4	−2003.347991	0.492895	−0.010205	3.7	0.1
M_1P_4-2,5	−2003.349676	0.493743	−0.009865	2.9	0.2
M_1P_4-3,5	−2003.349019	0.492247	−0.010494	2.8	0.3
o-M_2P_3	−2003.352997	0.493169	−0.009881	0.5	14.6

Table S1. (Continued)

Isomers[a]	E_{solv} (Hartree)[b]	G_{corr} (Hartree)[c]	TS_{corr}(Vib) (Hartree)[d]	ΔG_{soln} (kcal/mol)[e]	p_{soln} (%)[f]
o-M_2P_3-1	−2003.349738	0.491914	−0.010386	2.1	1.0
o-M_2P_3-2	−2003.350685	0.493143	−0.009925	2.0	1.2
o-M_2P_3-3	−2003.349976	0.492658	−0.010079	2.2	0.8
o-M_2P_3-4	−2003.348797	0.492548	−0.010222	3.0	0.2
o-M_2P_3-5	−2003.349673	0.493343	−0.009837	2.6	0.4
o-M_2P_3-1,3	−2003.349385	0.492414	−0.010624	2.5	0.5
o-M_2P_3-1,4	−2003.348635	0.493052	−0.010032	3.2	0.1
o-M_2P_3-2,4	−2003.352172	0.494168	−0.009780	1.6	2.4
o-M_2P_3-2,5	−2003.351693	0.493900	−0.009694	1.6	2.1
o-M_2P_3-3,5	−2003.350185	0.493516	−0.009800	2.4	0.6
m-M_2P_3	−2003.353433	0.492073	−0.010640	0.0	33.1
m-M_2P_3-1	−2003.350318	0.493956	−0.009879	2.7	0.4
m-M_2P_3-2	−2003.351526	0.493048	−0.009888	1.3	3.5
m-M_2P_3-3	−2003.351727	0.492967	−0.009969	1.2	4.3
m-M_2P_3-4	−2003.350654	0.493157	−0.009869	1.9	1.2
m-M_2P_3-5	−2003.350888	0.493472	−0.009998	2.1	1.0
m-M_2P_3-1,3	−2003.352376	0.494487	−0.009599	1.5	2.5
m-M_2P_3-1,4	−2003.351060	0.492514	−0.010271	1.5	2.5
m-M_2P_3-2,4	−2003.351610	0.493443	−0.009943	1.6	2.4
m-M_2P_3-2,5	−2003.352230	0.494180	−0.010271	1.8	1.5
m-M_2P_3-3,5	−2003.352912	0.493909	−0.009769	0.9	6.9

[a]See Figure S1 for nomenclature. [b]Energies calculated at M06-2X/6-311++g(3df,2p) level of theory (IEFPCM). [c]Thermal corrections at M06-2X/6-31+g(d,p) level of theory (IEFPCM). [d]Grimme's quasi-RRHO corrections of vibrational entropies. [e]Relative free energies in solution; $G_{solv} = E_{solv} + G_{corr} − TS_{corr}$(Vib). P_5 has 2-fold degeneracy and the others have 10-fold degeneracy. Enantiomers are included. [f]Relative populations of conformers.

Nomenclature
from *P* faces
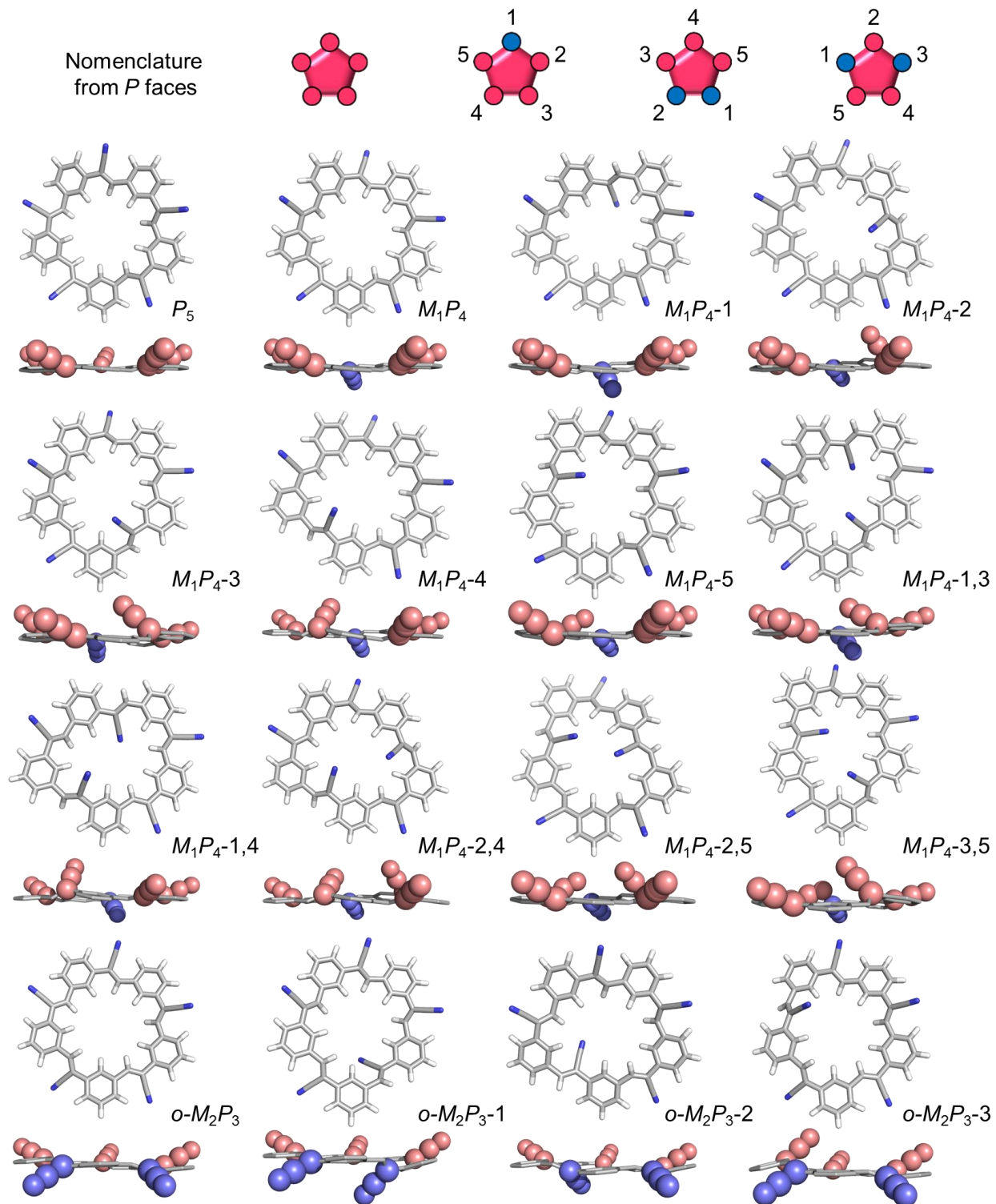
Figure S1. Optimized geometries of cyanostar conformers with global *P* chirality. In addition to using the sum of local chirality to describe the global state of bowl chirality, numbering rules are designed to describe the relative locations of cyano groups which have rolled into the cavity. The cyano groups are numbered clockwise when viewed from *P* faces of cyanostars. The priority of numbering has been given to cyano groups with *M* local chirality.

o-M$_2$P$_3$-4   *o*-M$_2$P$_3$-5   *o*-M$_2$P$_3$-1,3   *o*-M$_2$P$_3$-1,4

o-M$_2$P$_3$-2,4   *o*-M$_2$P$_3$-2,5   *o*-M$_2$P$_3$-3,5   *m*-M$_2$P$_3$

m-M$_2$P$_3$-1   *m*-M$_2$P$_3$-2   *m*-M$_2$P$_3$-3   *m*-M$_2$P$_3$-4

m-M$_2$P$_3$-5   *m*-M$_2$P$_3$-1,3   *m*-M$_2$P$_3$-1,4   *m*-M$_2$P$_3$-2,4

m-M$_2$P$_3$-2,5   *m*-M$_2$P$_3$-3,5
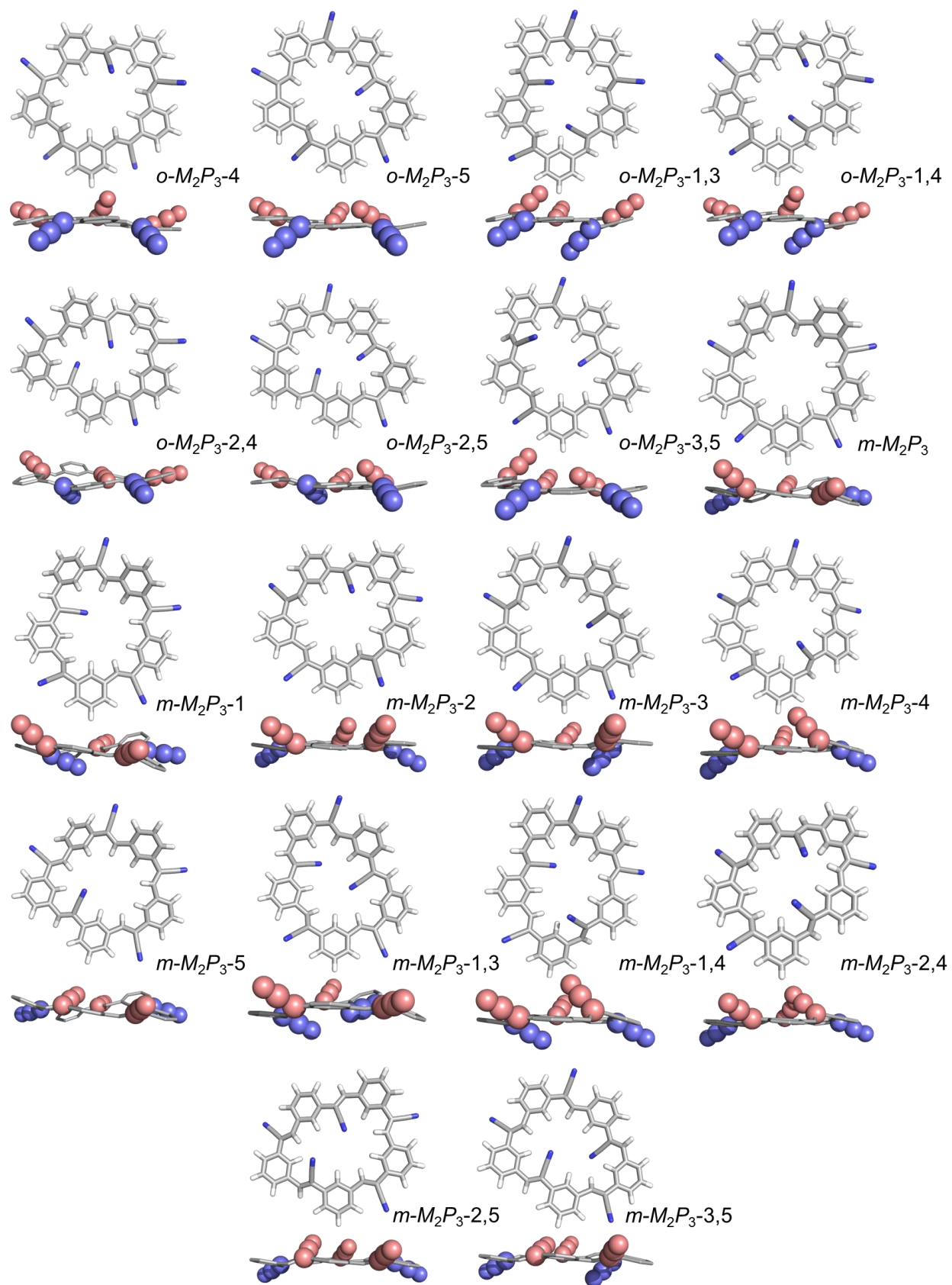
Figure S1. (Continued).

Table S2. Structural properties of DFT-optimized geometries of cyanostar conformers: dihedral angles (Φ) and root-mean-square deviations (RMSD).

Isomers	Φ_{CN} (degree)[a]	Φ_{CC} (degree)[a]	RMSD$_{soln}$ (Å)[b]	RMSD$_{xtal}$ (Å)[c]
P_5	23	−30	0.72	0
M_1P_4	18	−14	0.53	0.45
M_1P_4-1	−9	5	1.13	1.10
M_1P_4-2	39	−44	1.11	1.01
M_1P_4-3	37	−42	1.02	1.04
M_1P_4-4	36	−42	1.16	1.05
M_1P_4-5	39	−44	1.13	1.12
M_1P_4-1,3	13	−18	1.55	1.54
M_1P_4-1,4	10	−16	1.55	1.46
M_1P_4-2,4	61	−67	1.55	1.45
M_1P_4-2,5	62	−68	1.53	1.51
M_1P_4-3,5	62	−67	1.52	1.50
o-M_2P_3	4	−6	0.40	0.59
o-M_2P_3-1	−18	17	1.12	1.15
o-M_2P_3-2	−17	16	1.25	1.17
o-M_2P_3-3	29	−31	1.07	1.08
o-M_2P_3-4	26	−28	1.08	1.10
o-M_2P_3-5	40	−30	1.19	1.20
o-M_2P_3-1,3	6	−7	1.49	1.51
o-M_2P_3-1,4	2	−5	1.51	1.50
o-M_2P_3-2,4	11	61	1.69	1.73
o-M_2P_3-2,5	3	−5	1.61	1.60
o-M_2P_3-3,5	52	−55	1.55	1.55

Table S2. (Continued)

Isomers	Φ_{CN} (degree)[a]	Φ_{CC} (degree)[a]	RMSD$_{soln}$ (Å)[b]	RMSD$_{xtal}$ (Å)[c]
m-M_2P_3	6	−7	0	0.72
m-M_2P_3-1	−23	20	1.07	1.30
m-M_2P_3-2	30	−31	1.14	1.18
m-M_2P_3-3	−18	17	1.14	1.19
m-M_2P_3-4	28	−31	1.11	1.12
m-M_2P_3-5	30	−31	1.03	1.28
m-M_2P_3-1,3	23	49	1.61	1.71
m-M_2P_3-1,4	3	−6	1.55	1.54
m-M_2P_3-2,4	54	−56	1.55	1.55
m-M_2P_3-2,5	55	−56	1.53	1.62
m-M_2P_3-3,5	5	−6	1.55	1.64
Average[d]	10.3	−8.0	0.72	1.14

[a]Average dihedral angles within a conformer. [b]RMSD with regard to the most stable solution conformer, m-P_2M_3. [c]RMSD with regard to P_5 conformer, which is presented in the crystal structure of a typical 2:1 host-guest complex. [d]Boltzmann-weighted by p_{soln}.
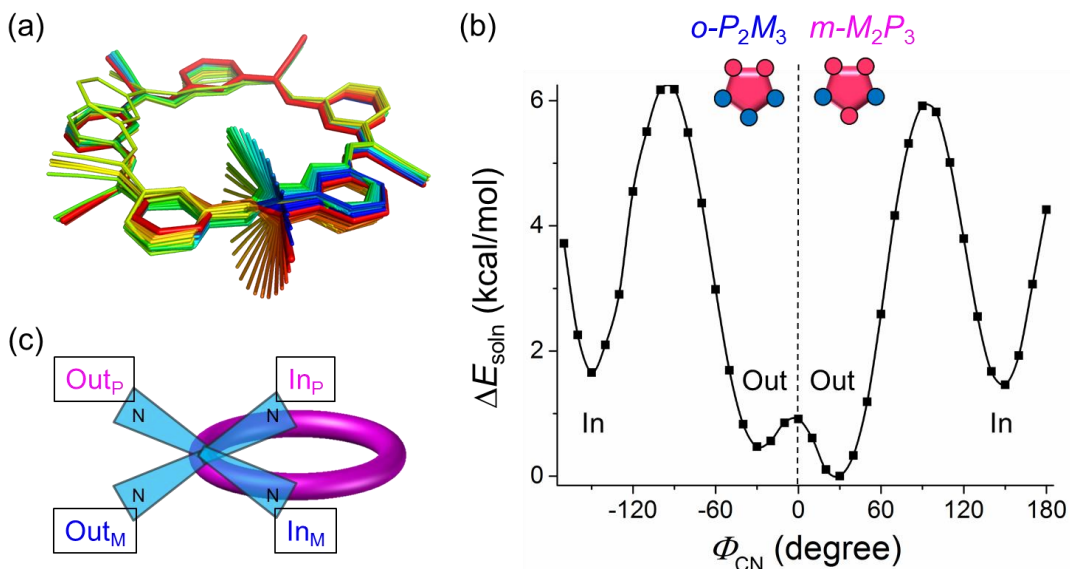
Figure S2. Relaxed PES scans for (a,b) PM<u>P</u>MP and (c) cartoon representation of rotamers. Hydrogen atoms are omitted for brevity.

Relaxed potential energy surface (PES) scans were performed to investigate representative torsion barriers of cyano-bearing olefins (Figures S2 and S3). Two different cyano-bearing olefin groups with P local chirality were chosen from the m-M_2P_3 conformer. Both scans were carried out by simultaneously increasing Φ_{CN} and Φ_{CC} with 10 ° step size from 0 ° to 180 ° in both positive and negative directions. Each geometry was relaxed at the M06-2X/6-31+g(d,p) level of theory with an additional step of single-point energy calculations with implicit solvation of CH_2Cl_2 (IEFPCM) at the same level of theory.
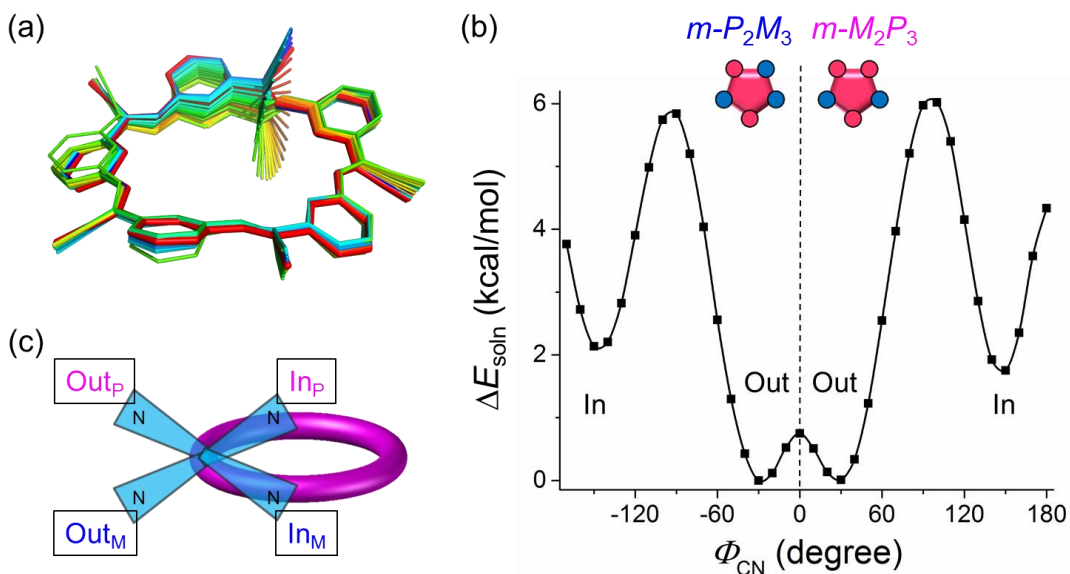
Figure S3. Relaxed PES scans for (a,b) PMPM*P* and (c) cartoon representation of rotamers. Hydrogen atoms are omitted for brevity.

The mathematically predicted 1024 conformations are not all energetically accessible. The reduction in number of conformers can be understood by the following observations. (1) At most, two cyano groups can exist as *in* rotamers at the same time, which will reduce the number to 512. (2) When two *in* rotamers are present, they must be *meta* to each other, reducing the number down to 352. The removed 160 conformers can be mathemetically derived. There are five possible choices for picking ortho positions in five-fold cyanostar. After that, each of the five olefins must be either *in* or *out*, both of which has two permutations, *up* and *down*. Thus, $5 \times 2^5 = 160$. (3) Rolling of cyano groups to the inside of a P_5 isomer always led to local inversions of neighbouring olefins, making one-*in* and two-*in* rotamers inaccessible (i.e., not local minima) for P_5 and M_5, which reduces the number to the final 332). The removed 20 conformers include five one-*in* rotamers and five *meta* two-*in* rotamers for P_5 and the same scenarios for M_5, respectively. Thus, $2 \times (5 + 5) = 20$.

S.2   Bowl Chirality of Cyanostar based on Dihedral Angles

Two issues associated with Szumna's[S5] nomenclature of bowl chirality needs to be addressed in order to extract structural information of cyanostars from MD simulations. **First**, cyanostar has changes in both local and global chirality. If a global reference is used, local chirality cannot be assigned. **Second**, the nomenclature depends on the priority principle of organic functional groups, which requires identification of the relative arrangement of these groups with regard to

the reference orientation for $>10^5$ geometries generated by MD simulations.

As a means to "read" out relative spatial information, dihedral angles are utilized to digitize local bowl chirality for olefins. By convention, a dihedral angle is positive when the four defining atoms are arranged in a right-handed helix, and *vice versa*. There are two flanking dihedral angles for each tilted cyano-bearing olefin above the macrocyclic plane. In particular, the two flanking dihedral angles are termed the CN dihedral angle, Φ_{CN}, and CC dihedral angle, Φ_{CC} (Figure S4a). For a *P* isomer with two neighboring phenyls coplanar, Φ_{CN} is positive, Φ_{CC} is negative, and the difference, $\Phi_{CN} - \Phi_{CC}$ remains positive (Figure S4); while for an *M* isomer under the same condition, all the signs are reversed.
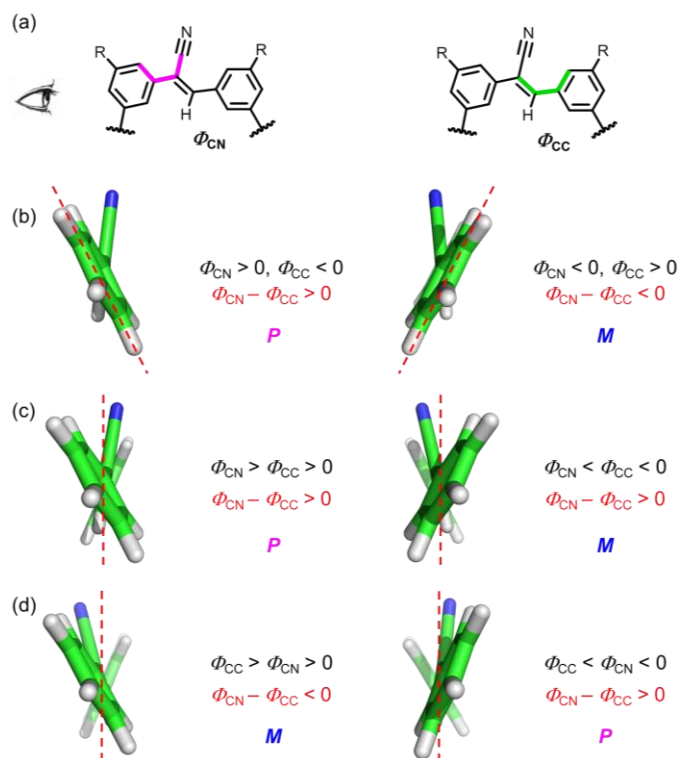
Figure S4. (a) Two flanking dihedral angles (Φ_{CN} and Φ_{CC}) were used to describe the orientations of cyano-bearing olefins relative to the reference planes (red dashed lines). All subsequent examples are shown as viewed from the left-hand side. Using the differences in dihedral angles, local chirality can be identified for (b) simple bowls and (c,d) complex bowls.

There is one important advantage of using the dihedral angle differences over individual dihedral angles: the cyanostar can be distorted so that the reference plane is no longer flat (Figure S4). Under this circumstance, the traditional nomenclature fails to identify bowl chirality. Thus, a new reference is proposed: a local plane instead of the macrocyclic plane. On account of the fact that each cyano group is located between its two flanking phenyl groups, a local reference can be defined as the tilting-angle-averaged plane of the two phenyl rings (Figure S4c and d, red dashed lines). With the new reference, the dihedral angle difference can still provide chirality assignments that are consistent with chemical intuition, while individual dihedral angle fails to, *e.g.*, when both dihedral angles are positive (Figure S4d). Specifically, there will be no local chirality if (1) the cyano group sits on the same plane as both flanking phenyl rings, *i.e.*, the

molecule is totally flat; or (2) the cyano group bifurcates the tilting angle between two flanking phenyl rings:

$$\text{if } \varPhi_{CN} - \varPhi_{CC} = 0, \text{ either (1) } \varPhi_{CN} = 0 \ \& \ \varPhi_{CC} = 0, \text{ or (2) } \varPhi_{CN} = \varPhi_{CC} \neq 0$$

The first scenario represents the conventional definition of bowl chirality: if the bowl is flat, there will be no bowl chirality. For the second scenario, the reference plane is now between the two flanking aromatic groups; if the cyano group sits on the reference plane, *i.e.*, bisecting the angle between the two neighbouring benzene rings, it would be considered locally flat and achiral for a bowl configuration. Overall, the first condition can be treated as a "classical bowl" on a flat plane while the second is a "complex bowl" on a curved plane.

S.3   General Procedures for MD Simulations

All simulations were performed with the MD software NAMD 2.9[S6] using the CHARMM force field for cyanostar as developed elsewhere.[S7] All the MD trajectories are generated in the constant pressure and constant temperature (NPT) ensemble. The systems were kept at constant temperature using Langevin dynamics for all non-hydrogen atoms with a Langevin damping coefficient of 5 ps^{-1}. Simulations were performed with an integration time step of 1 fs where bonded interactions were computed every time step, short-range non-bonded interactions every two time steps, and long range electrostatic interactions every four time steps. A cutoff of 16 Å was used for van der Waals (vdW) and short-range electrostatic interactions: a switching function was started at 15 Å for vdW interactions to ensure a smooth cutoff. Prior to simulation, each system was subjected to 1000 steps of conjugate gradient energy minimization followed by 100 ps of equilibration.
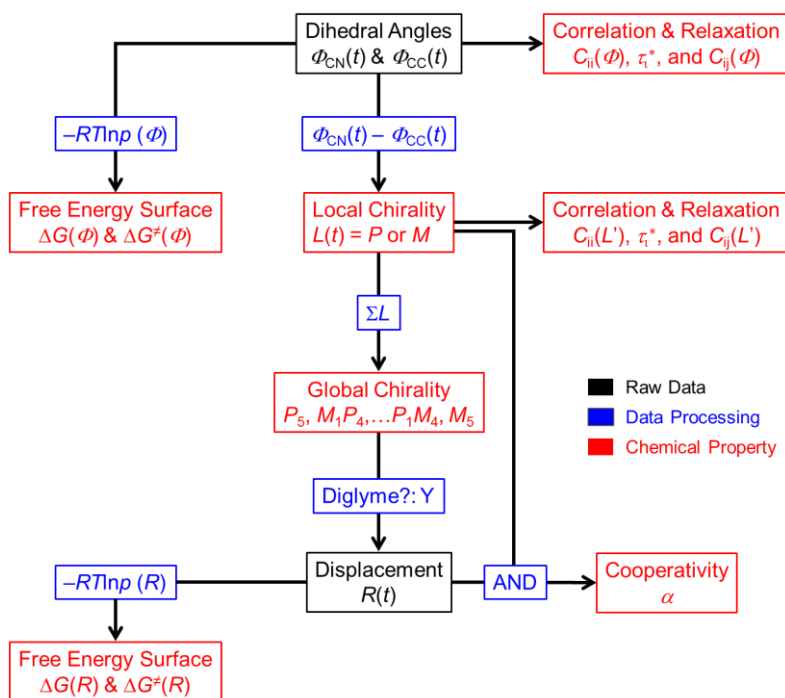

Figure S5. General workflow of data collection and processing to generate chemical properties.

General procedure of data processing is summarized here (Figure S5) and details are further described in each session. Two types of raw data were collected: dihedral angle data were always collected; when diglyme is present as the guest molecule, the displacement between the host, cyanostar, and the guest were also be collected. By calculating corresponding probability densities, both types of raw data were used to generate free energy surfaces with regard to the collective variables: dihedral angles (sections **S.4.3**, **S.5.1**, and **S.6.1**) and displacements (sections **S.5.2** and **S.6.2**). Based on the mathematical definition derived above (section **S.2**), the dihedral angles were digitized to identify both local and global bowl chirality of cyanostar at various conditions (sections **S.4.1**, **S.5.1**, and **S.6.1**). Further statistical analyses were performed on dihedral angles as well as chiral identities to reveal the dynamic stability of these variables (section **S.7**). For host-guest complexes, the chirality identities and displacements were combined to investigate how the presence of diglyme affects equilibrium distribution of stereoisomers of cyanostars (sections **S.5.2** and **S.6.2**).

S.4   MD Simulations of Single Cyanostars

An MD simulation was performed for a single cyanostar macrocycle at 298 K using an implicit dichloromethane solvent medium (ε_r = 8.9). The simulation was performed for 400 ns and structural parameters, Φ_{CN} and Φ_{CC}, were collected every 2 ps.

S.4.1   Bowl Chirality of Single Cyanostars

In this section, the detailed procedure to extract both local and global chirality of cyanostar monomers is described. On account of the fact that a cyanostar has five repeating olefins, five traces of CN dihedral angles and five traces of CC dihedral angles were generated; one representative examples of each case are included here (Figure S6). The simulation time was sufficiently long to produce the desirable equilibrium distribution that the populations of the enantiomers are identical (Figure S7). According to the dihedral angle differences ($\Phi_{CN} - \Phi_{CC}$, Figure S6), the local chirality (*L*, Figure S8) for each olefin group at a given frame can easily be coded by a truth table ($P = 0$, $M = 1$):

$$L(t) = \{-\text{Sign}[\Phi_{CN}(t) - \Phi_{CC}(t)] + 1\} \times 0.5$$

In reality, $\Phi_{CN} - \Phi_{CC}$ have a continuous distribution. The sign function converted this distribution to a simple, discrete distribution of (−1, 0, 1) by returning a value of −1 for negative numbers, 1 for positive numbers, and 0 for 0. Since almost all cyanostar isomers were observed to be chiral, Φ_{CN} was never observed to equal Φ_{CC}. Thus, the distribution was actually (−1, 1), and was shifted to (0, 1) by the expression: ((−1, 1) + 1) $\times 0.5$ = (0, 1). Based on this truth table, raw data can be easily digitized to reflect the local chirality changes, and be summed to define global chirality of cyanostar monomer. Basic statistics are summarized for a cyanostar monomer (Table S3).
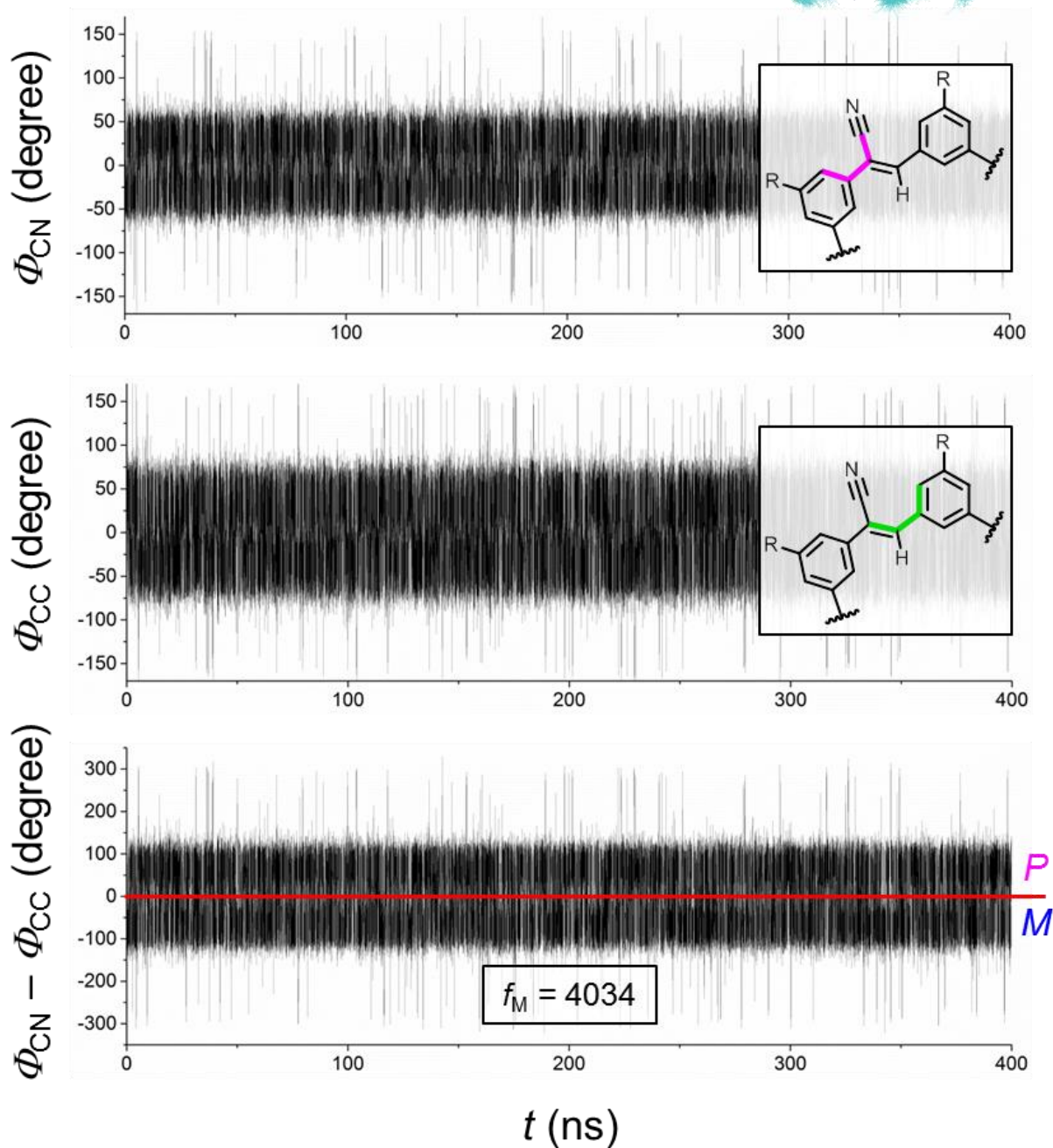
Figure S6. Representative trajectories of CN dihedral angles (Φ_{CN}), CC dihedral angles (Φ_{CC}), and dihedral angle differences ($\Phi_{CN} - \Phi_{CC}$) from a cyanostar monomer during the MD simulation (400 ns, 298 K). The number of *P*-to-*M* isomerization event, f_M, is noted.
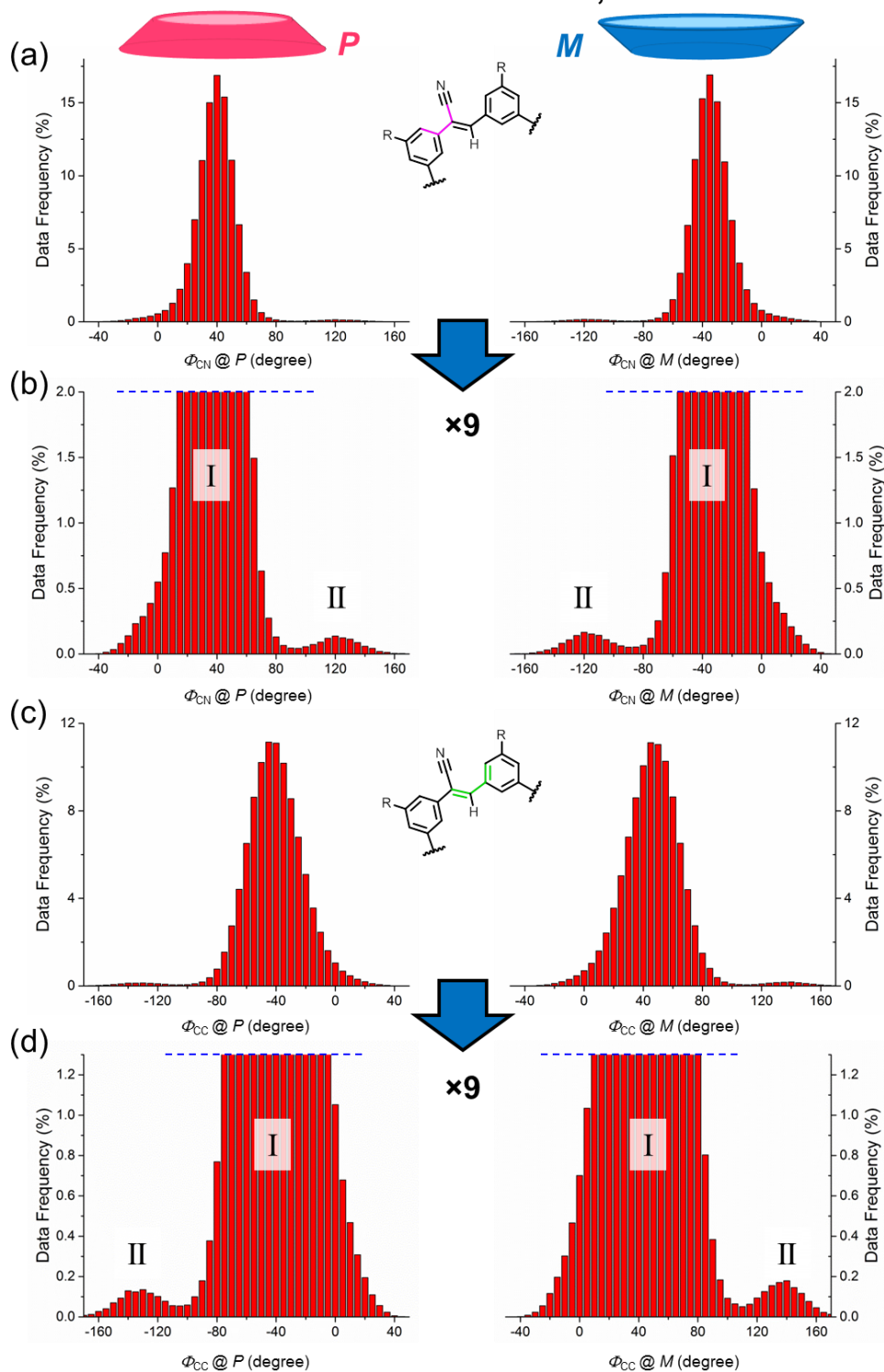
Figure S7. The equilibrium distributions of dihedral angles for (a) Φ_{CN} and (c) Φ_{CC} in a cyanostar monomer during the MD simulation (400 ns, 298 K), and the corresponding (b, d) amplified views. The distributions for *P* isomers are perfectly mirror images of those for *M* isomers. Local minima were notified by I and II.
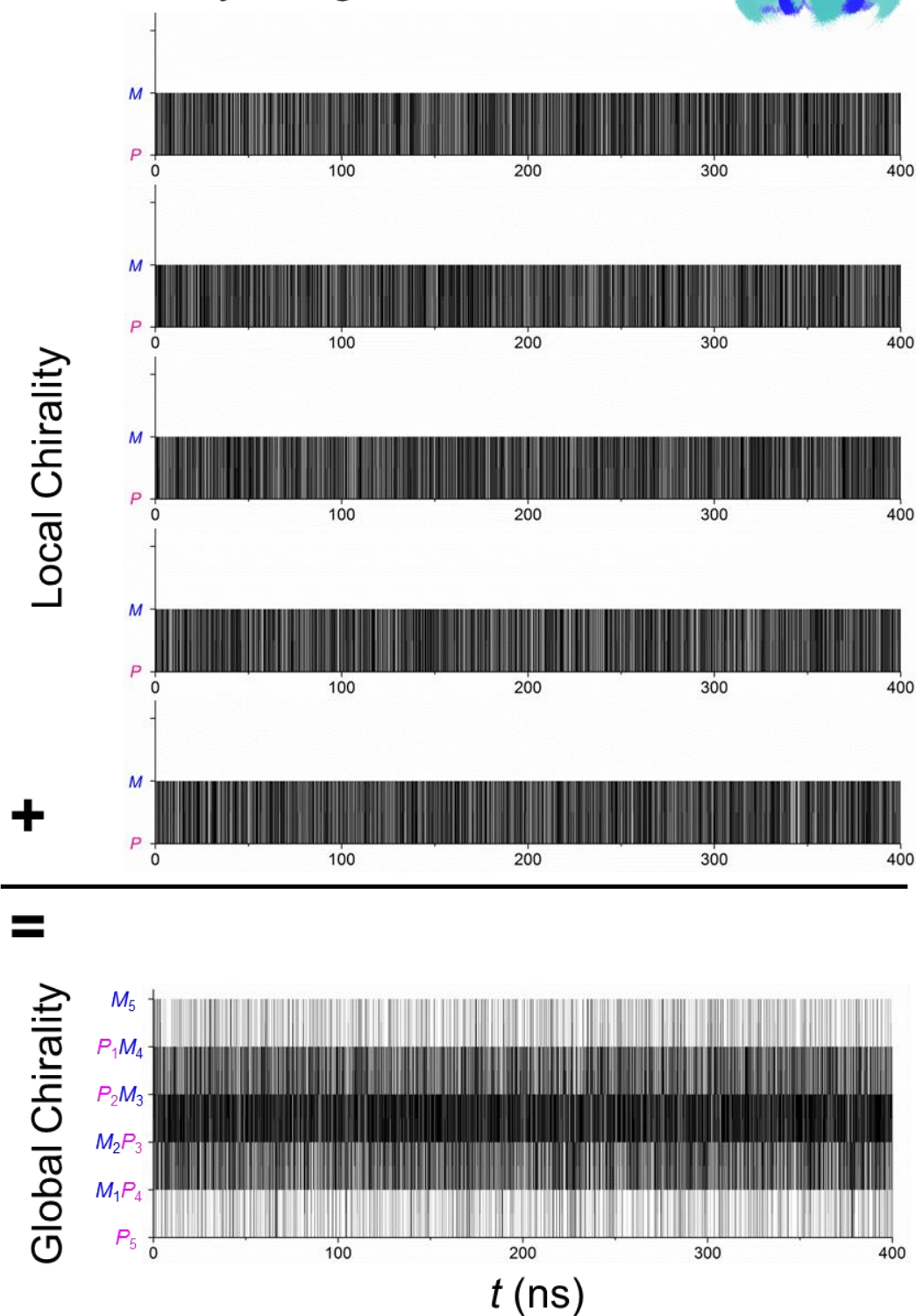
Figure S8. The trajectories of the local chirality assignments for five repeating olefins and their sum to the global chirality assignments of a cyanostar monomer during the MD simulation (400 ns, 298 K).

Table S3. Statistics of a cyanostar monomer (400 ns, 2 ps/frame, 298 K): dihedral angles (Φ), equilibrium distribution (F), and chirality inversions (f)

Trace #	Φ_{CN} (degree) [a]	Φ_{CC} (degree) [a]	F_M % [b]	f_{local} [c]
1	0 ± 41	0 ± 49	49.9	8068
2	0 ± 40	0 ± 49	50.4	7905
3	0 ± 40	0 ± 49	49.8	8086
4	0 ± 40	0 ± 49	49.7	8131
5	-1 ± 40	1 ± 48	51.0	7864
Average	0 ± 40	0 ± 49	50.2	8011
Chirality changes: 40054 local (10 ps, 100 GHz), 13602 global (29 ps, 35 GHz)				

[a]Based on Figure S6. [b]Percentage of frames that the M chirality emerges. [c]Number of times (frequencies) that an local chirality change occurs.

S.4.2 Bowl-bowl Inversion Pathways of Single Cyanostars

The major bowl-to-bowl inversion pathways are identified. The MD simulations of cyanostars in different scenarios showed that in most cases when a bowl inversion occurs in the cyanostar macrocycle, there is only one cyano group that changes its local chirality (Table S4). This finding allows for identification of major bowl-bowl inversion pathways using Δf_{global} data from an MD simulation (Table S5).
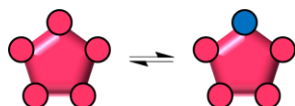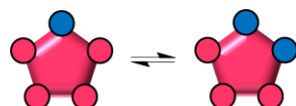
Table S4. Frequency of stereo-isomerizations (f_{global}) *vs.* local chirality changes (f_{local}).

	T (K)	$\sum f_{local}$ [a]	f_{global} [b]	$\sum f_{local} / f_{global}$
	178	200	200	1.00
Dimer	218	618	617	1.00
	298	16006	15191	1.05
Monomer	298	40054	34961	1.14
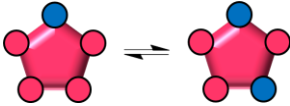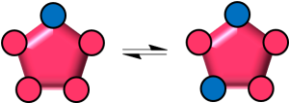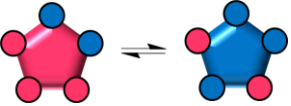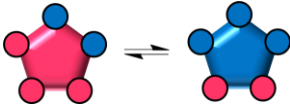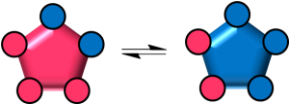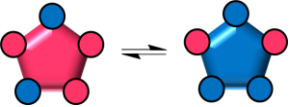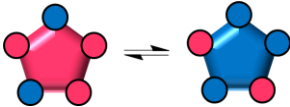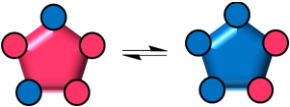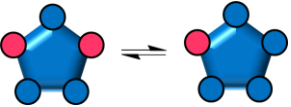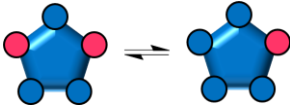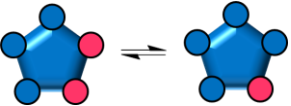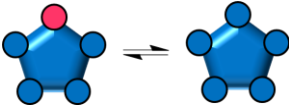
[a]Sums of number of times that a local chirality changes over five traces of local chirality $L(t)$. [b]Number of times that the global chirality, $\Sigma L(t)$, changes.

Table S5. Statistics of the stereoisomerization pathways of a cyanostar monomer at 298 K.

Pathways [a]	P_5 to M_1P_4		M_1P_4 to $o\text{-}M_2P_3$		M_1P_4 to $o\text{-}M_2P_3$	
f_{local} [b]	967	964	963	962	888	872
Reactions						

Table S5. (Continued)

Pathways [a]	M_1P_4 to m-M_2P_3		M_1P_4 to m-M_2P_3		o-M_2P_3 to m-M_3P_2	
f_{local} [b]	1004	1018	1054	1029	954	930
Reactions						
Pathways [a]	o-M_2P_3 to o-M_3P_2		o-M_2P_3 to o-P_2M_3		m-M_2P_3 to m-M_2P_3	
f_{local} [b]	960	987	1094	1065	1001	1025
Reactions						
Pathways [a]	m-M_2P_3 to m-P_2M_3		m-M_2P_3 to o-P_2M_3		m-P_2M_3 to P_1M_4	
f_{local} [b]	1031	993	1001	984	1085	1064
Reactions						
Pathways [a]	m-P_2M_3 to P_1M_4		o-P_2M_3 to P_1M_4		o-P_2M_3 to P_1M_4	
f_{local} [b]	1032	982	928	951	1023	1040
Reactions						
Pathways [a]	P_1M_4 to M_5					
f_{local} [b]	1034	5357				
Reactions						

[a]Pathways that changes molecular bowl chirality are colored in red. [b]Number of times that a local chirality changes. The first value corresponds to the forward reaction, and the second corresponds to the backward reaction.

S.4.3 Olefin Rotations in Single Cyanostars

Here, dihedral angles (Φ) are used instead of chirality identities (L) to delineate free energy landscape for rotamers and to obtain barriers of olefin rotations (Table S6). Different from section **S.4.1**, rotamers (Figure S9) are now considered as reactants and products in the equilibrium processes: In_P, Out_P, Out_M, and In_M.

Table S6. Thermodynamics and kinetics of olefin rotations in a cyanostar monomer at 298 K.

Pathways [a]	In_M to Out_M		Out_M to Out_P		Out_P to In_P	
ΔG_{rot} (kcal mol^{-1}) [b]	−2.6		0		2.7	
$\Delta G_{rot}^{\neq}$ (kcal mol^{-1}) [c]	0.7	3.4	1.5	1.5	3.5	0.7

[a]The In_M-to-In_P pathway was not observed during the MD simulation. [b]Based on Figure S9 using Φ_{CN}. [c]Based on Figure S9 using Φ_{CN}; the first column corresponds to forward activation barriers, and the second corresponds to backward activation barriers.

Table S7. Equilibrium distribution of dihedral angles in a cyanostar monomer at 298 K.[a]

Rotamer	P		M	
	Φ_{CN} (degree)	Φ_{CC} (degree)	Φ_{CN} (degree)	Φ_{CC} (degree)
Out	37 ± 11	-44 ± 17	-37 ± 11	44 ± 17
In	118 ± 16	-134 ± 17	-115 ± 15	134 ± 15

[a]Errors of the dihedral angles were identified by peak widths based on Figure S7.
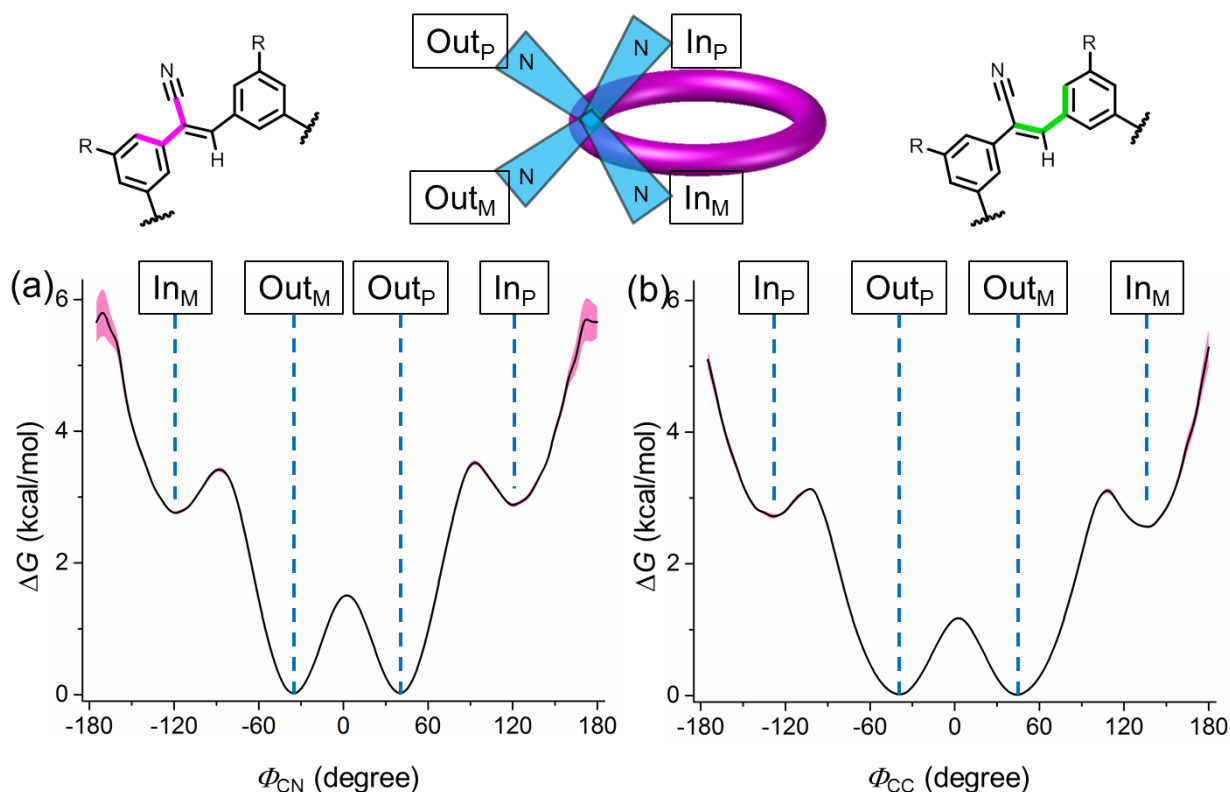
Figure S9. The free energy surfaces for olefin rotations in a cyanostar monomer using (a) CN and (b) CC dihedral angles. Errors are shown as pink areas.

For a cyanostar monomer, Φ_{CN} and Φ_{CC} are distributed around four local minima (Figure S7, Table S7), which is consistent with the relaxed PES scans done by DFT (Figures S2 and S3).

To create a free energy surface, probability mass functions[S8] were computed for the distributions of dihedral angles with a bin size of 5 ° (Figure S9). One caution must be taken here in choosing the bin size: high resolution choice, *i.e.*, very small bin size compared to total data available, may lead to insufficient data and high noise level in some bins. The errors of free energy calculations were estimated by the variance when bootstrapping repeatedly 50% of the data.[S9]

S.5   Transition States for Cyanostar Bowl-bowl Inversions: DFT Calculation

The initial geometries for transition states were obtained by quick PES scans at the lower M06-2X/6-31g(d) level of theory (IEFPCM) on the internal coordinates of interest , Φ_{CN}. The highest energy geometries extracted from the scans were further optimized as transition states to obtain thermal corrections and energies. The transition states were verified by observations (1) that each transition state has only one imaginary frequency that corresponds to Φ_{CN} rocking motions of interest, and (2) that minimum energy structures were re-obtained by following the intrinsic reaction coordinates from the transition states forward or backward. Enantiomers of these transition states are not duplicated here. The results are summarized in Tables S8 and S9, and coordinates in the appended *Cyanostar Transition States.mol*.

Table S8. DFT characterizations on transition states for olefin rocking motions.

Transition States[a]	E_{solv} (Hartree)[b]	G_{corr} (Hartree)[c]	TS_{corr}(Vib) (Hartree)[d]	ΔG_{soln} (kcal/mol)[e]
M_1P_4-1	−2003.351117	0.494683	−0.009458	2.4
M_1P_4-2	−2003.351697	0.494269	−0.009569	1.8
M_1P_4-3	−2003.352361	0.494342	−0.009493	1.4
M_1P_4-4	−2003.352359	0.492359	−0.009444	1.6
M_1P_4-5	−2003.351713	0.495155	−0.009243	2.1
Following pathways invert the global bowl chirality				
o-M_2P_3-3	−2003.351894	0.491894	−0.009506	1.6
o-M_2P_3-4	−2003.352536	0.494593	−0.009403	1.8
o-M_2P_3-5	−2003.351905	0.494791	−0.009298	1.4
m-M_2P_3-4	−2003.352511	0.493943	−0.009859	1.3

[a]See Figure S10 for nomenclature, "ts" is omitted for clarity. [b]Energies calculated at M06-2X/6-311++g(3df,2p) level of theory using IEFPCM implicit solvation. [c]Thermal corrections at M06-2X/6-31+g(d,p) level of theory using IEFPCM implicit solvation. [d]Grimme's quasi-RRHO corrections of vibrational entropies. [e]Relative free energies in solution to m-M_2P_3; $G_{solv} = E_{solv} + G_{corr} - TS_{corr}$(Vib). All transition states have 10-fold degeneracy, and enantiomers are included.
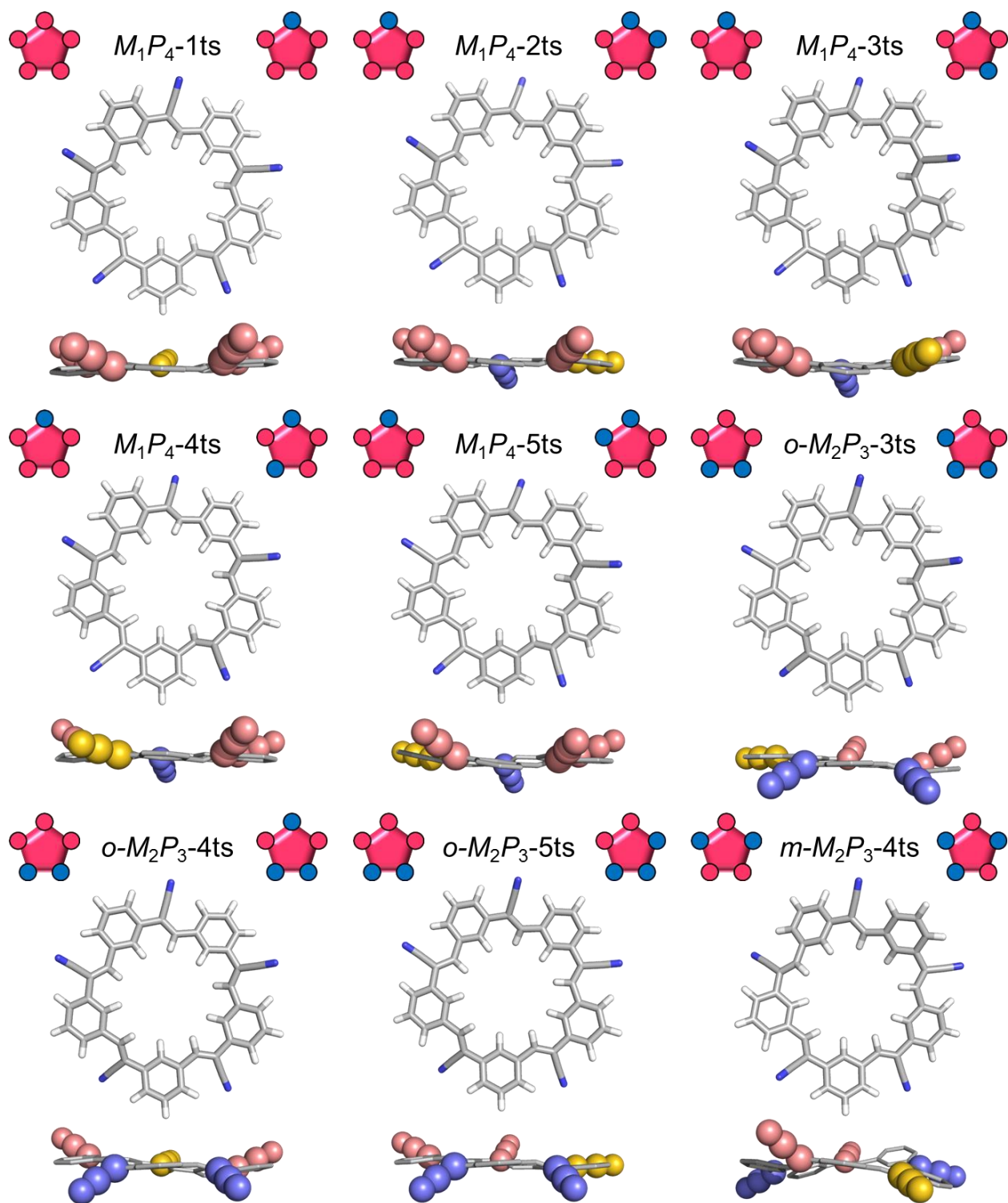
Figure S10. Optimized transition state geometries of cyanostar along the rocking-based bowl inversion pathways. While local *P* chirality is colored in pink and *M* in blue, the transitioning local chirality is colored in yellow. Both the reactant and the product, which two are connected by the transition state, were shown in cartoon representations.

Table S9. Summary of DFT calculations of cyanostar isomers with implicit solvation of CH_2Cl_2.

Transition States[a]	$\Phi_{CN}^{\ddagger}$ (degree)[b]	Reactant	$\Delta G_{soln,for}^{\ddagger}$ (kcal/mol)[c]	Product	$\Delta G_{soln,rev}^{\ddagger}$ (kcal/mol)[d]
M_1P_4-1	5.0	P_5	0.7	M_1P_4	1.8
M_1P_4-2	−0.6	M_1P_4	1.2	o-M_2P_3	1.3
M_1P_4-3	5.9	M_1P_4	0.8	m-M_2P_3	1.4
M_1P_4-4	6.6	M_1P_4	1.0	m-M_2P_3	1.6
M_1P_4-5	−1.3	M_1P_4	1.6	o-M_2P_3	1.6
Following pathways invert the global bowl chirality					
o-M_2P_3-3	0.2	o-M_2P_3	1.1	o-P_2M_3	1.1
o-M_2P_3-4	4.0	o-M_2P_3	0.9	m-P_2M_3	1.4
o-M_2P_3-5	0.7	o-M_2P_3	1.3	o-P_2M_3	1.3
m-M_2P_3-4	0.3	m-M_2P_3	1.3	m-P_2M_3	1.3

[a]See Figure S10 for nomenclature, "ts" is omitted for clarity. [b]Dihedral angles of the inverting olefins at the transition state. [c]Barriers of forward reactions. [d]Barriers of backward reactions.

S.6 MD Simulations of 1:1 Cyanostar-Diglyme Complexes

An MD simulation was performed for a single cyanostar macrocycle, bearing a diglyme as the guest molecule at 298 K. Dihedral angles were collected using the same protocol described in section **S.5**.

S.6.1 Bowl Chirality of Cyanostars in 1:1 Cyanostar-Diglyme Complexes

The same protocol described in section **S.4.1** was used to analyze the dihedral angles collected from the MD simulation (Table S10).

Table S10. Statistics of a cyanostar monomer in a 1:1 cyanostar-diglyme complex (400 ns, 2 ps/frame, 298 K): dihedral angles (Φ), equilibrium distribution (F), and chirality inversions (f).

Trace #	Φ_{CN} (°)[a]	Φ_{CC} (°)[a]	F_M %[b]	f_{local}[c]
1	0 ±40	0 ±48	50.5	8482
2	0 ±40	0 ±48	50.3	8687
3	0 ±41	0 ±48	50.2	8605
4	0 ±40	0 ±48	50.4	8621
5	0 ±40	0 ±48	49.8	8567
Average	0 ±40	0 ±48	50.2	8592
42962 local (9.3 ps, 110 GHz), 14051 global (28 ps, 35 GHz)				

[a]Based on Figure S11. [b]Percentage of frames in which an M isomer emerges. [c]Number of times that an local chirality changes.
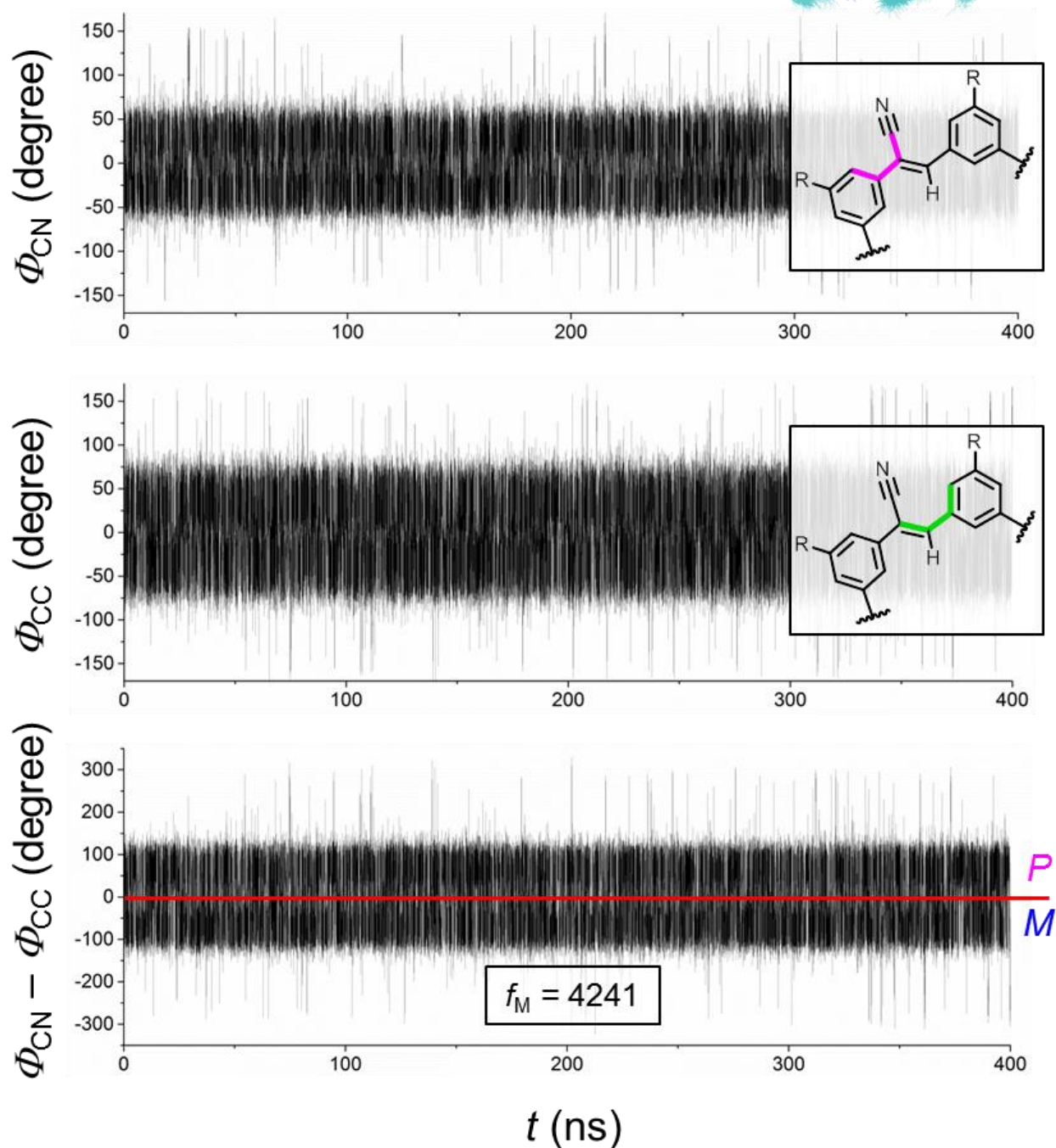
Figure S11. Representative trajectories of CN dihedral angles (Φ_{CN}), CC dihedral angles (Φ_{CC}), and dihedral angle differences ($\Phi_{CN} - \Phi_{CC}$) from a cyanostar monomer within a 1:1 cyanostar-diglyme complex during the MD simulation (400 ns, 298 K). The number of *P*-to-*M* isomerization event, f_M, is noted.
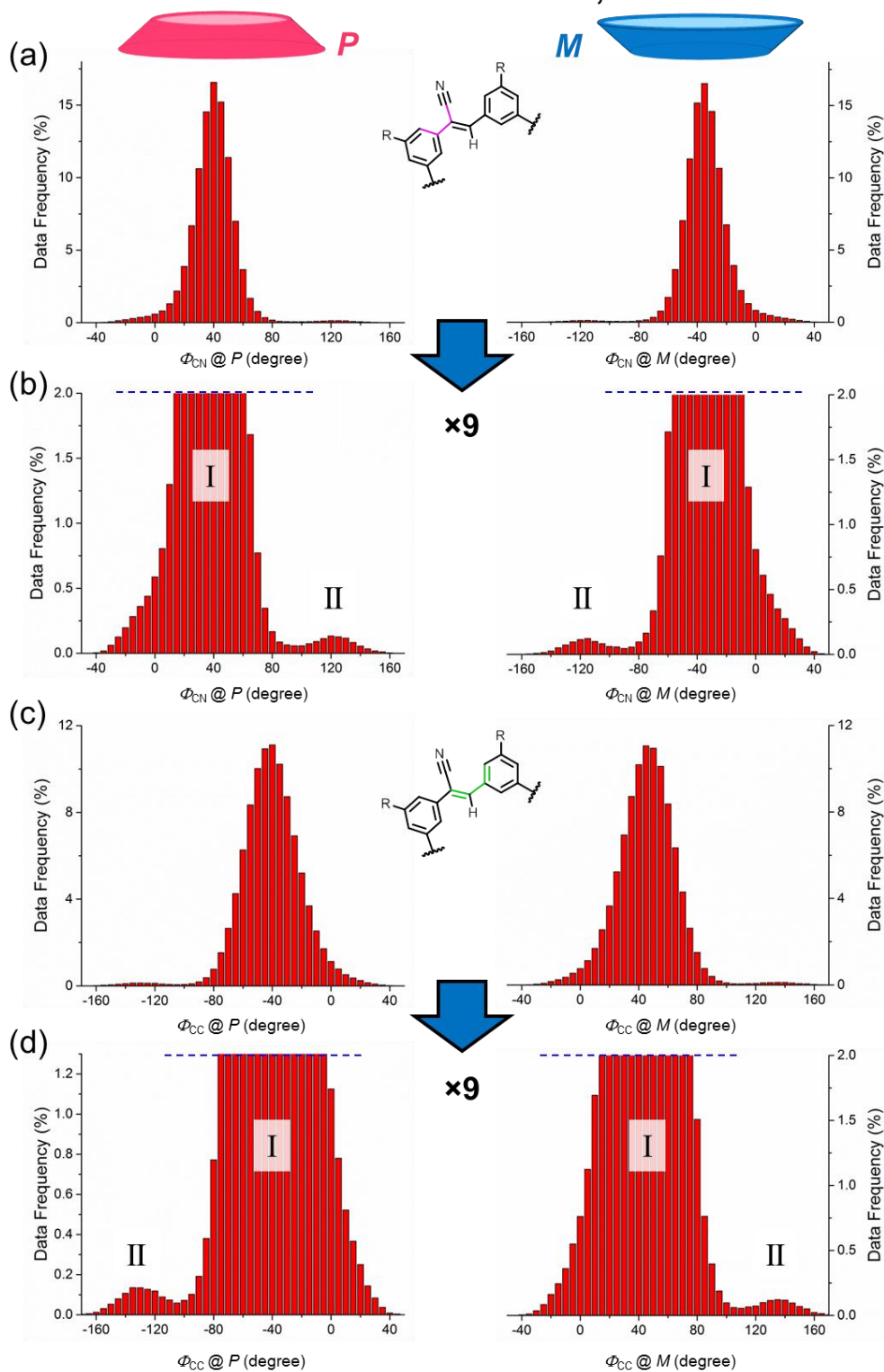
Figure S12. The equilibrium distributions of dihedral angles for (a) Φ_{CN} and (c) Φ_{CC} from a cyanostar monomer within a 1:1 cyanostar-diglyme complex during the MD simulation (400 ns, 298 K), and the corresponding (b, d) amplified views. Local minima were notified by I and II.
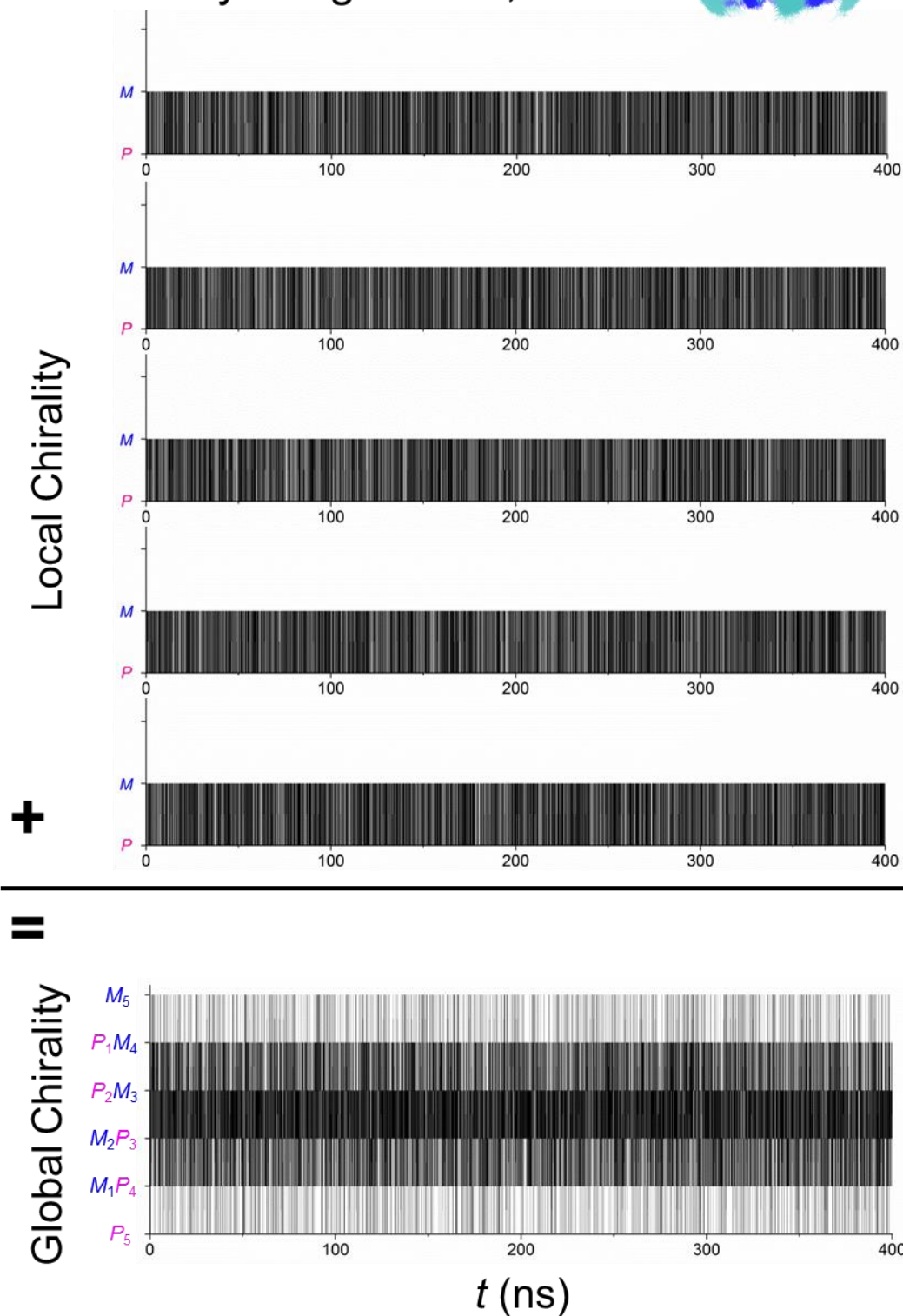
Figure S13. The trajectories of the local chirality assignments for five repeating olefins and their sum to the global chirality assignments of a cyanostar monomer during the MD simulation (400 ns, 298 K).

Table S11. Equilibrium positions of dihedral angles of a cyanostar monomer within a 1:1 cyanostar-diglyme complex at 298 K.[a]

Rotamer	P		M	
	Φ_{CN} (degree)	Φ_{CC} (degree)	Φ_{CN} (degree)	Φ_{CC} (degree)
Out	38 ± 12	-44 ± 20	-38 ± 12	44 ± 20
In	118 ± 17	-131 ± 20	-118 ± 17	131 ± 20

[a]Errors of the dihedral angles were identified by peak widths based on Figure S12.

Table S12. Thermodynamics and kinetics of olefin rotations in a cyanostar monomer at 298 K.

Pathways [a]	*In*$_M$ to *Out*$_M$		*Out*$_M$ to *Out*$_P$		*Out*$_P$ to *In*$_P$	
ΔG_{rot} (kcal mol^{-1}) [b]	-2.9		0		2.9	
$\Delta G_{rot}^{\neq}$ (kcal mol^{-1}) [c]	0.6	3.5	1.5	1.5	3.4	0.5

[a]The *In*$_M$-to-*In*$_P$ pathways was not observed during the MD simulation. [b]Based on Figure S14 using Φ_{CN}. [c]Based on Figure S14 using Φ_{CN}; the first column corresponds to forward activation barriers, and the second corresponds to backward activation barriers.
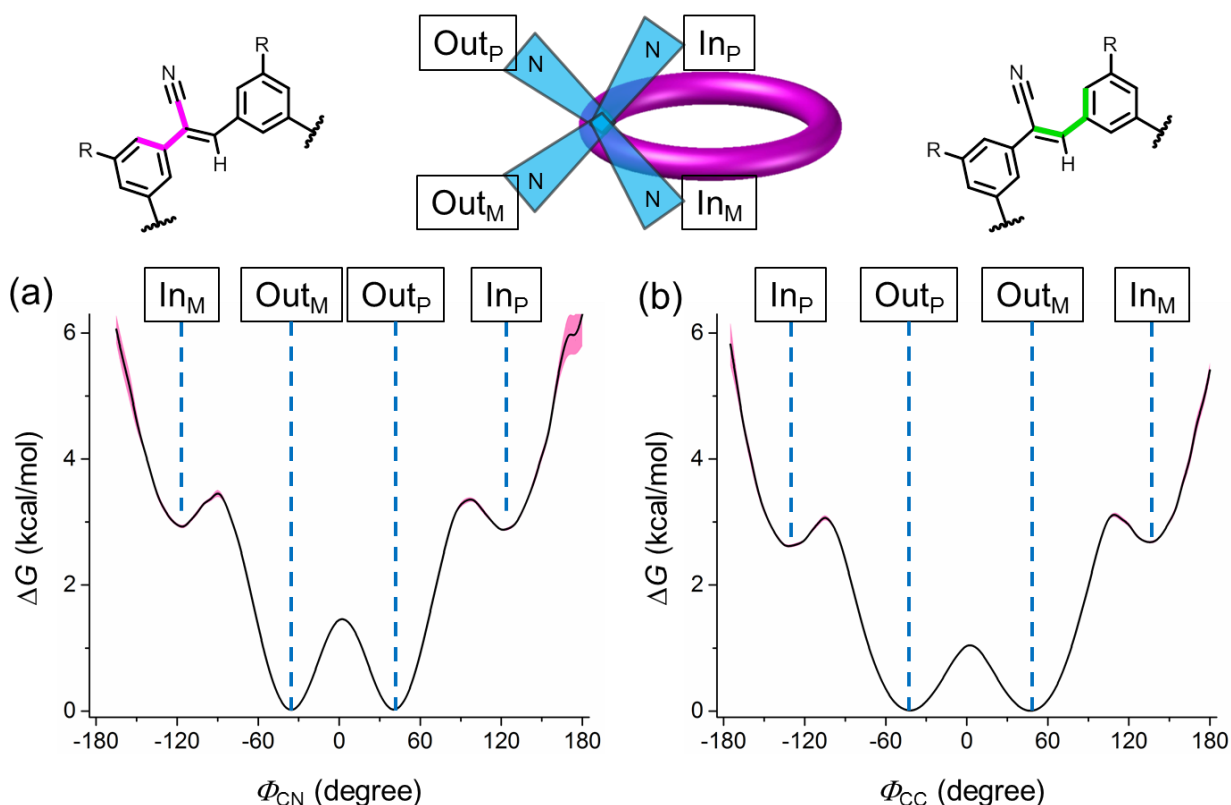
Figure S14. The free energy surfaces for olefin rotations in a cyanostar monomer within a 1:1 cyanostar-diglyme complex using (a) CN and (b) CC dihedral angles. Errors are shown as pink areas.

S.6.2 Diglyme Binding to Single Cyanostars

In this section, the host-guest interactions between the guest, diglyme, and the host, cyanostar monomer, were investigated. Intermolecular displacements, R, between the center of the diglyme $(\bar{x}, \bar{y}, \bar{z})$ and the center of a cyanostar monomer $(\bar{x'}, \bar{y'}, \bar{z'})$ were collected every 2 ps (Figure S15). The MD simulation was performed for 400 ns using implicit CH_2Cl_2 solvent media.

Diglyme displacements, 298 K

$\bar{R} = 2.5 \pm 1.8$ Å
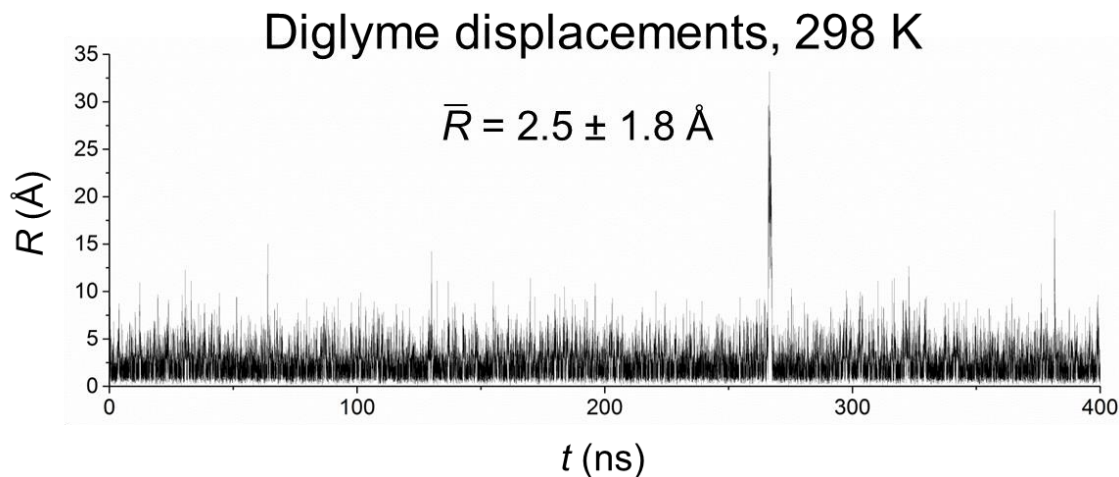
Figure S15. The trajectory of intermolecular displacements, R, between diglyme and a cyanostar monomer during the simulation (298 K, 400 ns).

Displacement distributions, 298 K
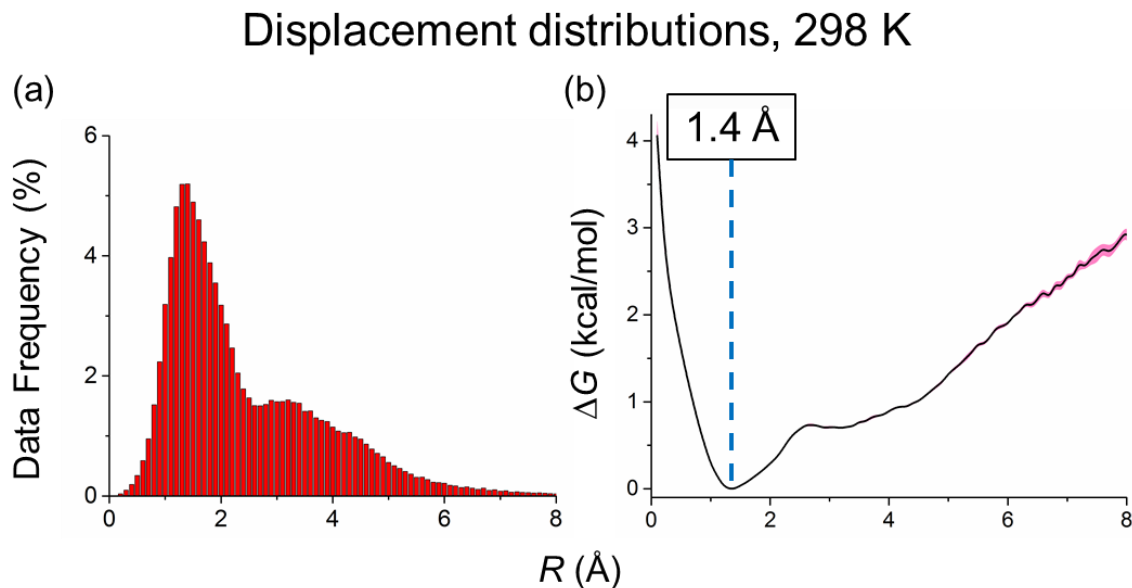
Figure S16. (a) The distribution of diglyme displacement, R, relative to the center of the cyanostar monomer at 298 K and (b) corresponding free energy surface. Errors are shown as pink areas.

The free energy surface was constructed by probability mass functions[S8] using a bin size of 0.1 Å. The thermodynamics were not directly derived from the free energy surface on account of the following facts: (1) not all degrees of freedom are obtained, such as rotations; (2)

displacements are not the best parameters for comprehensive description of interactions between diglyme, a rod, and cyanostar, a bowl.

S.6.3   Impact of Hydrogen Bonding to Changing Landscape of 1:1 Complexes

This impact of hydrogen bonding is evaluated by to which extent the conformational landscape changs when the diglyme has exited the binding cavity. To quantify such shift, two processes are imagined: diglyme binding equilibrium and a bowl-to-bowl inversion equilibrium between a hypothetical state including all other conformations and the global minimum, m-P_2M_3 and m-P_3M_2. If the host-guest interactions have no effect, this hypothetical equilibrium will not change; if the interaction does have effect, escape of guest will reverse the landscape of the bound state to that of the unbound state, leading to an increase of the hypothetical equilibrium constant, K, for the bowl inversion (global minimum is at the denominator). The degree of increase is evaluated by ratio, α, defined as the following:

$$\alpha = K_{iso}(\text{Free}) / K_{iso}(\text{Dig})$$

First, a boundary, Γ, was defined based on the intermolecular displacement of diglyme, R, to distinguish whether diglyme is bound to cyanostar or not:

$$\Gamma = [\text{Sign}(R - R_0) + 1] \times 0.5, \text{ where } R_0 = 3, 6, 9 \text{ Å}.$$

The boundary displacement, R_0, was chosen to be larger than the 2.4 Å binding radius of the cyanostar dimer; multiple boundaries are included for completeness's sake. Specifically, if the diglyme appears outside the boundary, the corresponding frame will be labelled with a value of **1**.

Second, the identity of conformers, $\sum$, must be labeled to distinguish global minima, m-P_2M_3 and m-P_3M_2, from other conformers. To only know the number of P and M is insufficient to identify all isomers on account of the fact that there are two isomers with P_2M_3 chirality and two with P_3M_2. To uniquely digitize every isomer, the following expressions were used:

Recall that the local chirality is digitized as: $L = [-\text{Sign}(\Phi_{CN} - \Phi_{CC}) + 1] \times 0.5$

Sum the local chirality to obtain the global chirality: $\sum_{global} = \sum L_i$ ($n = 5$, $i = 1$)

Differentiate o- and m-isomer: $\sum_{diff} = \sum |L_i - L_j|$ ($n = 5$, $i = 1$, $i \neq j$)

Define unique identities (I) for all isomers: $I = (\sum_{global})^2 + \sum_{diff}$

The $\sum_{global}$ term will provide the following values for each isomer: $P_5 = 0$, $P_4M_1 = 1$, o-$P_3M_2 = 2$, m-$P_3M_2 = 2$, o-$P_2M_3 = 3$, m-$P_2M_3 = 3$, $P_1M_4 = 4$, $M_5 = 5$; while $\sum_{diff}$ will produce: $P_5 = 0$, $P_4M_1 = 2$, o-$P_3M_2 = 2$, m-$P_3M_2 = 4$, o-$P_2M_3 = 2$, m-$P_2M_3 = 4$, $P_1M_4 = 2$, $M_5 = 0$. $\sum_{diff}$ gives different values for o- and m-isomer but cannot differentiate global P and M chirality. To combine $\sum_{diff}$ and $\sum_{global}$ using an arbitrary but nonlinear manner, the unique identities are obtained: $P_5 = 0$, $P_4M_1 = 3$, o-$P_3M_2 = 6$, m-$P_3M_2 = 8$, o-$P_2M_3 = 11$, m-$P_2M_3 = 13$, $P_1M_4 = 18$, $M_5 = 25$. Thus, the

number of frames used in the determination of $\sum$ was obtained by removing those frames with a unique identity value of either 8 (m-P_3M_2) or 13 (m-P_2M_3):

$$\sum = \text{Sign}\{|(I-8) \times (I-13)|\}$$

If conformers other than m-P_2M_3 or m-P_3M_2 occur in the frame, the corresponding frame will be labelled with a value of **1**.

Equilibrium constants for bowl inversions can thus be expressed using the labels for conformer identity ($\sum$) and boundary of diglyme binding (Γ):

$$K_{\text{iso}}(\text{Free}) = F(\textstyle\sum = 1; \Gamma = 1) / F(\textstyle\sum = 0; \Gamma = 1)$$

$$K_{\text{iso}}(\text{Dig}) = F(\textstyle\sum = 1; \Gamma = 0) / F(\textstyle\sum = 0; \Gamma = 0)$$

The results of α under different Γ are summarized in Table S13.

Table S13. Cooperativity (α) between local chirality changes and diglyme debinding in a cyanostar monomer.

R_0 (Å)^a	K_{iso}(Free)	K_{iso}(Dig)	α
3	2.09	2.05	1.0
6	1.98	2.06	1.0
9	2.10	2.06	1.0

S.7 MD Simulations of 2:1 Cyanostar-Diglyme Complexes

MD simulations were performed for cyanostar dimers bearing a diglyme molecule as the guest at 298, 218, and 178 K, using an implicit dichloromethane solvent medium (ε_r = 8.9, 12.3 and 16.4, respectively). The simulations were performed for 800 ns at 178 K, and 400 ns at 218 K and 298 K. All dihedral angles were collected every 2 ps. Achieving a symmetrical distribution of diglyme above and below the dimer was used as a criterion for estimating the minimum time for an MD simulation. The time-averaged structure of one macrocycle over a sufficiently long period of time has the same statistical features as the other macrocycle in a dimer. This statistical relationship is perhaps best understood by the point symmetry elements these dimers possess: an inversion center in a *meso* dimer (M-P) and a C_2 axis in a homochiral dimer (M-M and P-P). Therefore, the analysis of two types of dihedral angles, Φ_{CN} and Φ_{CC}, and the chirality information are represented by a P isomer within an M-P dimer.

S.7.1 Bowl Chirality of Cyanostars in 2:1 Cyanostar-Diglyme Complexes

The *homo*-chiral and *meso* dimers show high similarity during MD simulations (section **S.7.4**). Based on this observation and the assumption of point symmetries, the detailed analysis on dihedral angles was done on one cyanostar macrocycle of a *meso*-dimer. The same protocol

(section **S.4.1**) was followed to reveal both local and global information of cyanostar's bowl chirality at various temperatures (Figures S19, S21, and S23). Using the truth table derived in section **S.4.1**, dihedral angles and chirality information (Figure S17) can be easily digitized and are summarized for MD simulations run at different temperatures (Table S14).

Table S14. Bowl Inversions of a *P* cyanostar isomer in an *M-P* dimer at different temperatures.

T	M_1P_4		M_2P_3		P_2M_3		P_1M_4	
	F^a	ΔG (kcal/mol)^b	F	ΔG (kcal/mol)	F	ΔG (kcal/mol)	F	ΔG (kcal/mol)
178 K	711	2.2	2	4.3^c	0	-	0	-
	Chirality changes: 200 local (4 ns, 0.25 GHz), 0 global.							
218 K	1344	2.2	6	4.5^c	0	-	0	-
	Chirality changes: 618 local (0.6 ns, 2 GHz), 0 global.							
298 K	28228	1.1	2533	2.5	137	4.2	6	6.1^c
	Chirality changes: 16006 local (12 ps, 80 GHz), 178 global (1 ns, 1 GHz)							

^{a}Number of frames that the corresponding conformer emerges. $^b\Delta G = -RT\ln(F_j\ /\ F_{P5})$. ^{c}Insufficient data and may be associated with large errors.

Table S15. Thermodynamics and kinetics of olefin rocking motions on the *P* cyanostar macrocycles within the 2:1 *M-P* cyanostar-diglyme complexes at different temperatures.

	T (K)	178		218		298	
	ΔG (kcal mol^{-1})	Φ_{CN}	Φ_{CC}	Φ_{CN}	Φ_{CC}	Φ_{CN}	Φ_{CC}
In_P-Out_P	Integration ^{a}	$-$ ^{d}	$-$ ^{d}	–3.8	–3.9	–4.0	–3.8
	FES ^{b}	$-$ ^{d}	$-$ ^{d}	–4.0	–3.8	–4.0	–3.8
	$\Delta\overline{G}$ (kcal mol^{-1})	$-$ ^{d}		–3.9		–3.9	
	$\Delta G^{\neq}$ (kcal mol^{-1}) ^{c}	$-$ ^{d}	$-$ ^{d}	4.9	4.9	4.8	4.3
	$\Delta\overline{G}^{\neq}$ (kcal mol^{-1})	$-$ ^{d}		4.9		4.5	
Out_M-Out_P	Integration	–2.9	–2.9	–2.8	–3.0	–2.0	–2.1
	FES ^{b}	–3.0	–3.0	–3.1	–3.0	–2.2	–2.1
	$\Delta\overline{G}$ (kcal mol^{-1})	–2.9		–2.9		–2.0	
	$\Delta G^{\neq}$ (kcal mol^{-1}) ^{c}	3.3	3.0	3.4	3.1	2.4	2.2
	$\Delta\overline{G}^{\neq}$ (kcal mol^{-1})	3.2		3.2		2.3	

$^a\Delta G = -RT\ln K$, where $K_{ij} = F_j\ /\ F_i$. ^{b}Free energy surface. ^{c}The barriers were reported for the reversed reactions, *i.e.*, Out_P-In_P and Out_P-Out_M. ^{d}Not observed.
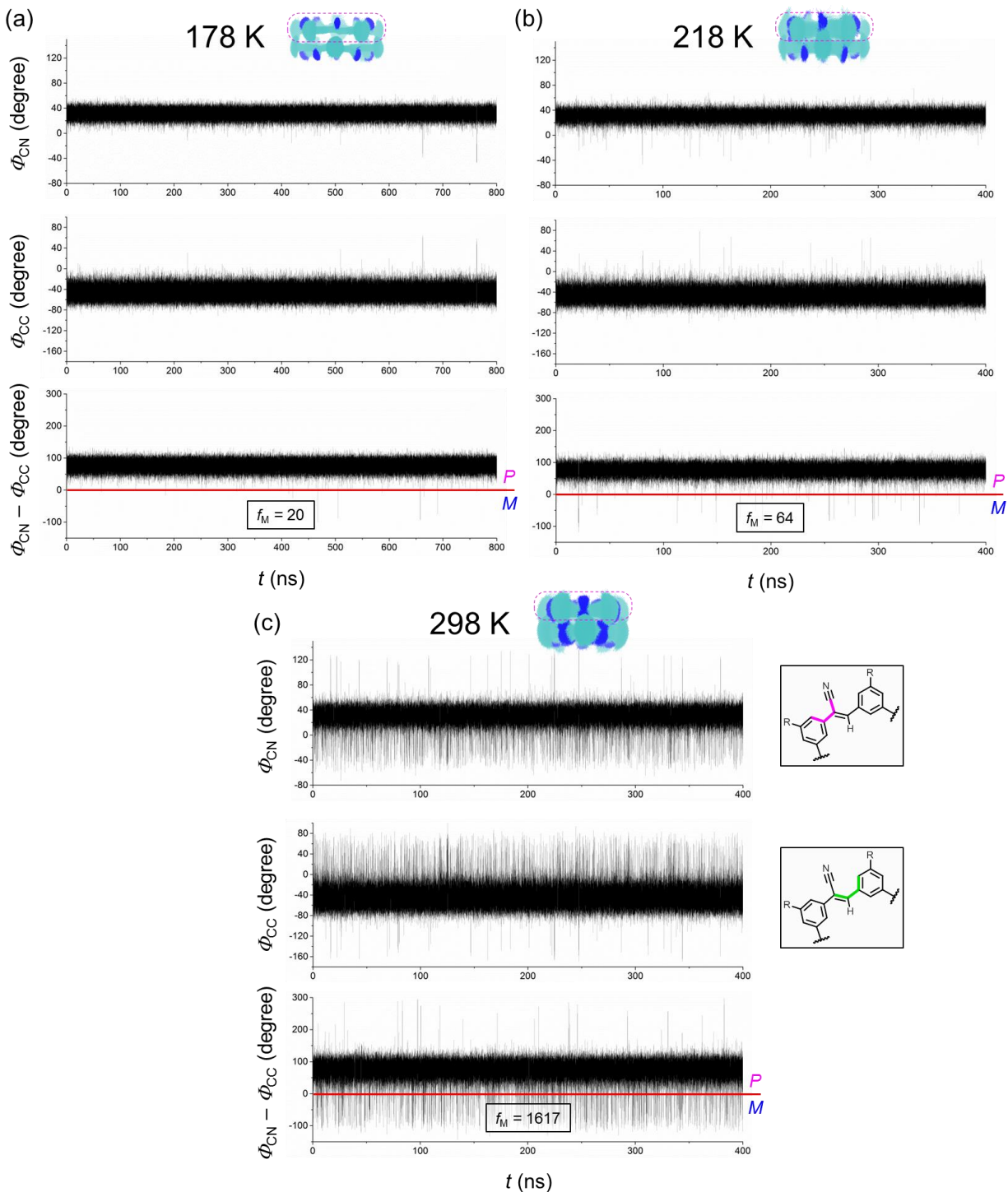
Figure S17. Representative trajectories of CN dihedral angles (Φ_{CN}), CC dihedral angles (Φ_{CC}), and dihedral angle differences ($\Phi_{CN} - \Phi_{CC}$) from the P cyanostar macrocycles within the 2:1 M-P cyanostar-diglyme complexes during the MD simulations at (a) 178 K, 800 ns; (b) 218 K, 400 ns; (c) 298 K, 400 ns. The numbers of P-to-M isomerization event, f_M, are noted.

Dihedral distributions, 178 K
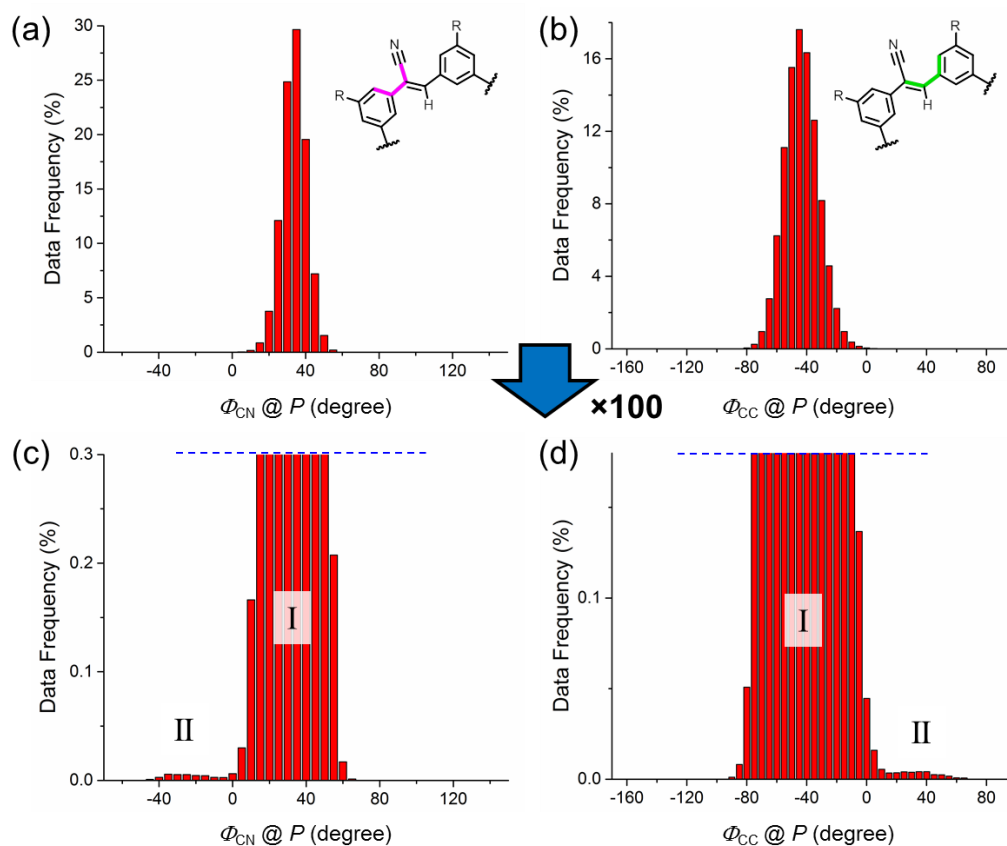
Figure S18. The equilibrium distributions of dihedral angles for (a) Φ_{CN} and (b) Φ_{CC}, and the corresponding (c, d) amplified views. Local minima were notified by I and II.

Table S16. Statistics of dihedral angles for the *P* cyanostar macrocycle within the 2:1 *M-P* cyanostar-diglyme complex (800 ns, 2 ps/frame, 178 K): dihedral angles (Φ), equilibrium distribution (F) and kinetics of local chirality inversions (f).

	Statistics [a]				Free Energy Surface [b]		
Trace #	Φ_{CN} (degree)	Φ_{CC} (degree)	F_M [c]	f_{local} [d]	Rotamer	Φ_{CN} (degree)	Φ_{CC} (degree)
1	31 ± 7	-46 ± 12	206	22	Out_P	34 ± 7	-44 ± 11
2	31 ± 7	-46 ± 11	104	40	In_P	-25 ± 25	34 ± 16
3	31 ± 7	-46 ± 12	283	40			
4	31 ± 7	-46 ± 11	88	58			
5	31 ± 7	-46 ± 11	34	40			
Average	31 ± 7	-46 ± 11	143	40			

[a]Based on Figure S17. [b]Based on Figure S24. [c]Number of frames that the *M* chirality emerges. [d]Number of times (frequencies) that an local *P*-to-*M* or *M*-to-*P* isomerization occurs.

Figure S19. The trajectories of the local chirality assignments for five olefins and their sum to the global chirality assignments for the *P* cyanostar macrocycle in the 2:1 *M-P* cyanostar-diglyme complex during the MD simulation (800 ns, 178 K).
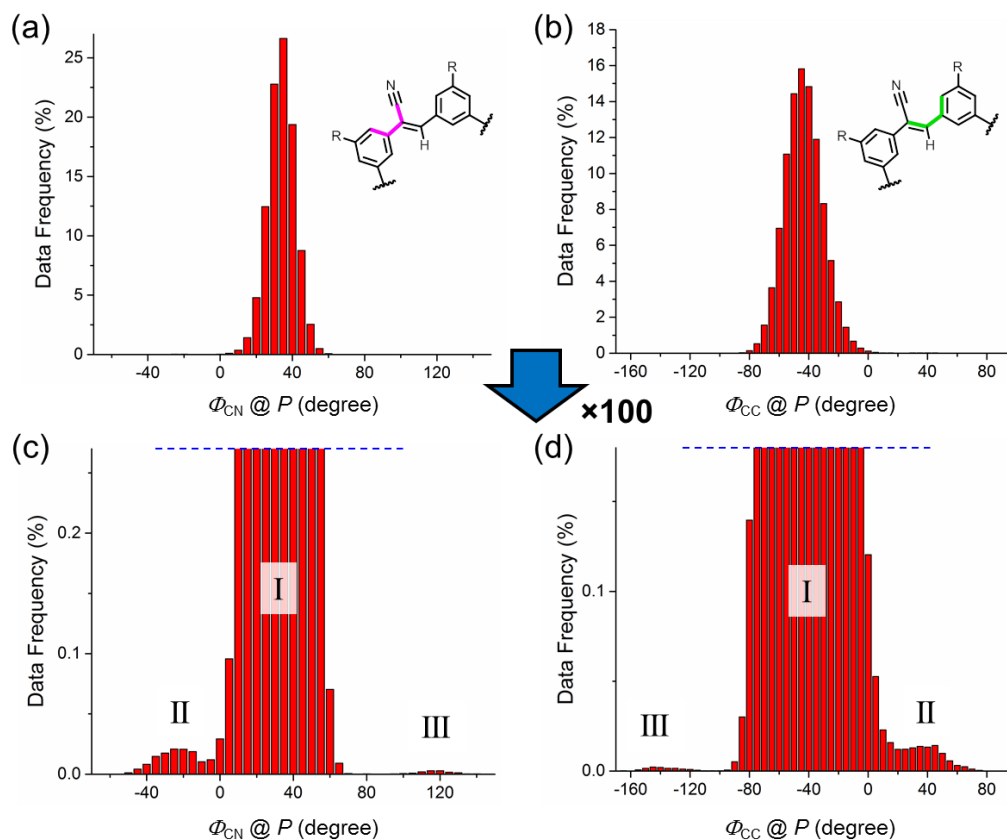
Figure S20. The equilibrium distributions of dihedral angles for (a) Φ_{CN} and (b) Φ_{CC}, and the corresponding (c, d) amplified views. Local minima were notified by I and II.

Table S17. Statistics of dihedral angles for the *P* cyanostar macrocycle within the 2:1 *M-P* cyanostar-diglyme complex (400 ns, 2 ps/frame, 218 K): dihedral angles (Φ), equilibrium distribution (*F*) and kinetics of local chirality inversions (*f*).

	Statistics[a]				Free Energy Surface[b]		
Trace #	Φ_{CN} (degree)	Φ_{CC} (degree)	F_M[c]	f_{local}[d]	Conformer	Φ_{CN} (degree)	Φ_{CC} (degree)
1	31 ± 8	-46 ± 13	138	102	Out_P	34 ± 7	-44 ± 12
2	31 ± 8	-46 ± 13	383	116	Out_M	-23 ± 12	34 ± 18
3	31 ± 8	-46 ± 13	321	134	In_P	117 ± 8	-139 ± 24
4	31 ± 8	-46 ± 13	216	138			
5	31 ± 8	-46 ± 13	298	128			
Average	31 ± 8	-46 ± 13	271	124			

[a]Based on Figure S17. [b]Based on Figure S24. [c]Number of frames that the *M* chirality emerges. [d]Number of times (frequencies) that an local *P*-to-*M* or *M*-to-*P* isomerization occurs.
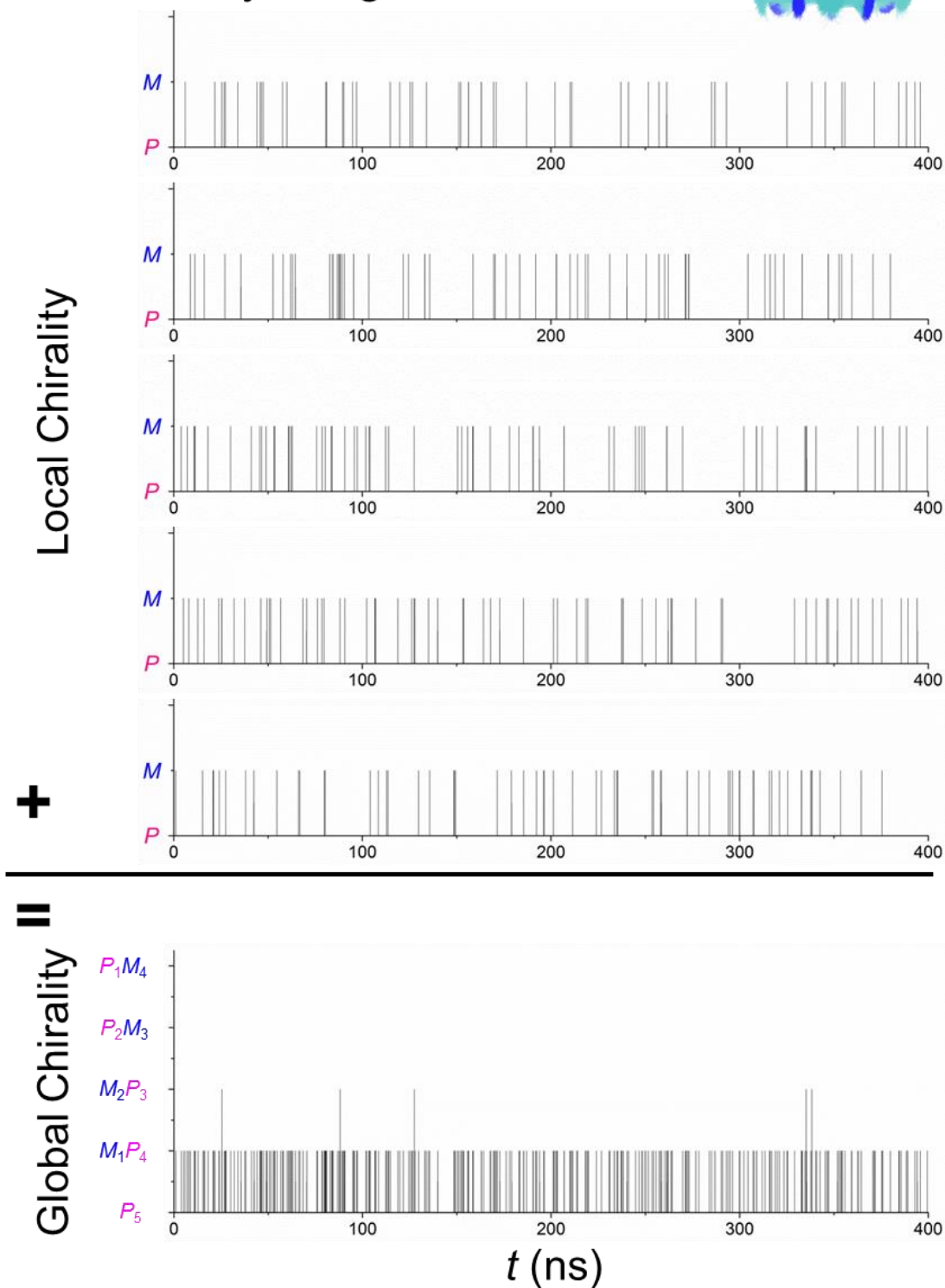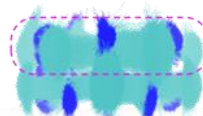
Figure S21. The trajectories of the local chirality assignments for five olefins and their sum to the global chirality assignments for the *P* cyanostar macrocycle in the 2:1 *M-P* cyanostar-diglyme complex during the MD simulation (400 ns, 218 K).

Dihedral distributions, 298 K
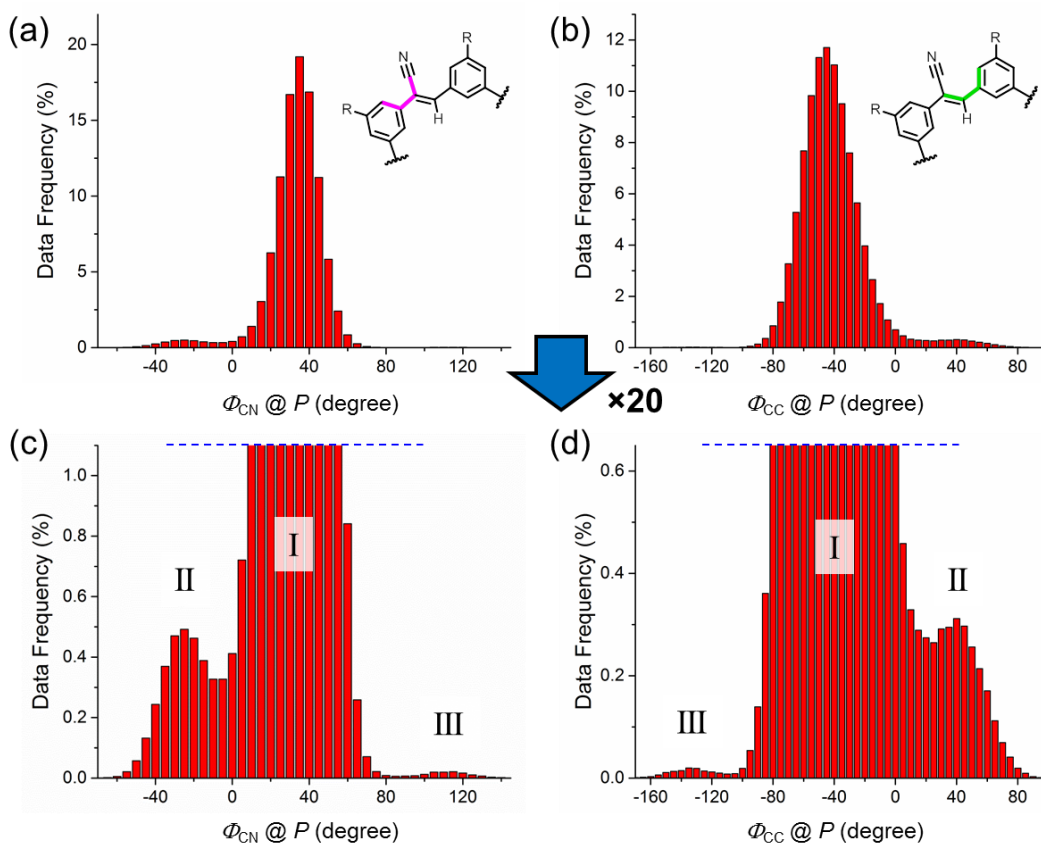
Figure S22. The equilibrium distributions of dihedral angles for (a) Φ_{CN} and (b) Φ_{CC}, and the corresponding (c, d) amplified views. Local minima were notified by I and II.
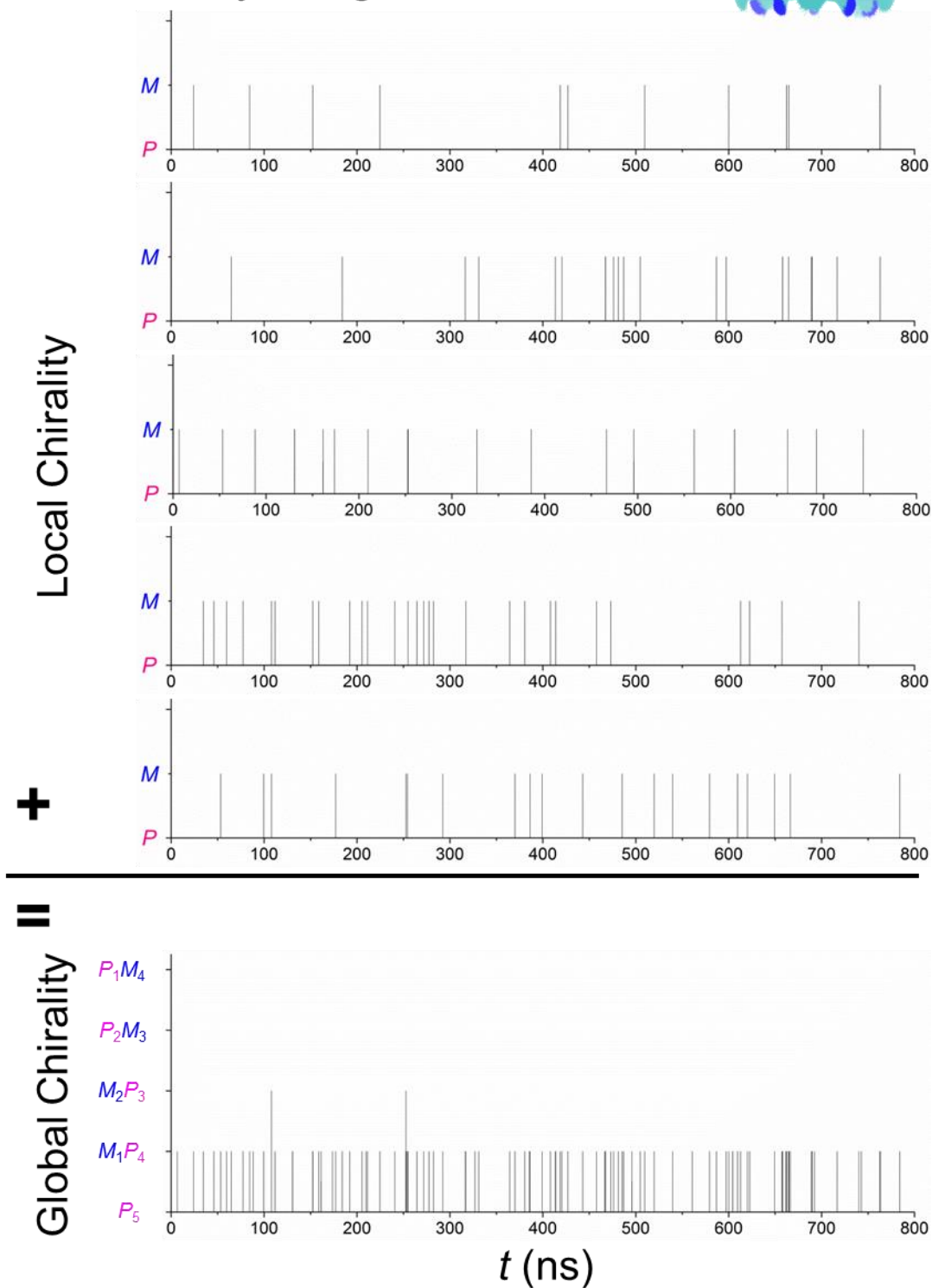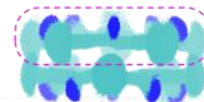
Table S18. Statistics of dihedral angles for the *P* cyanostar macrocycle within the 2:1 *M-P* cyanostar-diglyme complex (400 ns, 2 ps/frame, 298 K): dihedral angles (Φ), equilibrium distribution (F) and kinetics of local chirality inversions (f).

	Statistics[a]				Gaussian Peak Fitting[b]		
Trace #	Φ_{CN} (degree)	Φ_{CC} (degree)	F_M[c]	f_{local}[d]	Conformer	Φ_{CN} (degree)	Φ_{CC} (degree)
1	30 ± 15	-44 ± 22	6576	3234	Out_P	35 ± 10	-45 ± 16
2	30 ± 15	-43 ± 22	6860	3126	Out_M	-22 ± 15	38 ± 20
3	30 ± 15	-43 ± 22	7346	3328	In_P	111 ± 11	-133 ± 16
4	30 ± 15	-44 ± 22	6626	3182			
5	30 ± 15	-44 ± 22	6321	3136			
Average	30 ± 15	-44 ± 22	6746	3201			

[a]Based on Figure S17. [b]Based on Figure S24. [c]Number of frames that the *M* chirality emerges. [d]Number of times (frequencies) that an local *P*-to-*M* or *M*-to-*P* isomerization occurs.
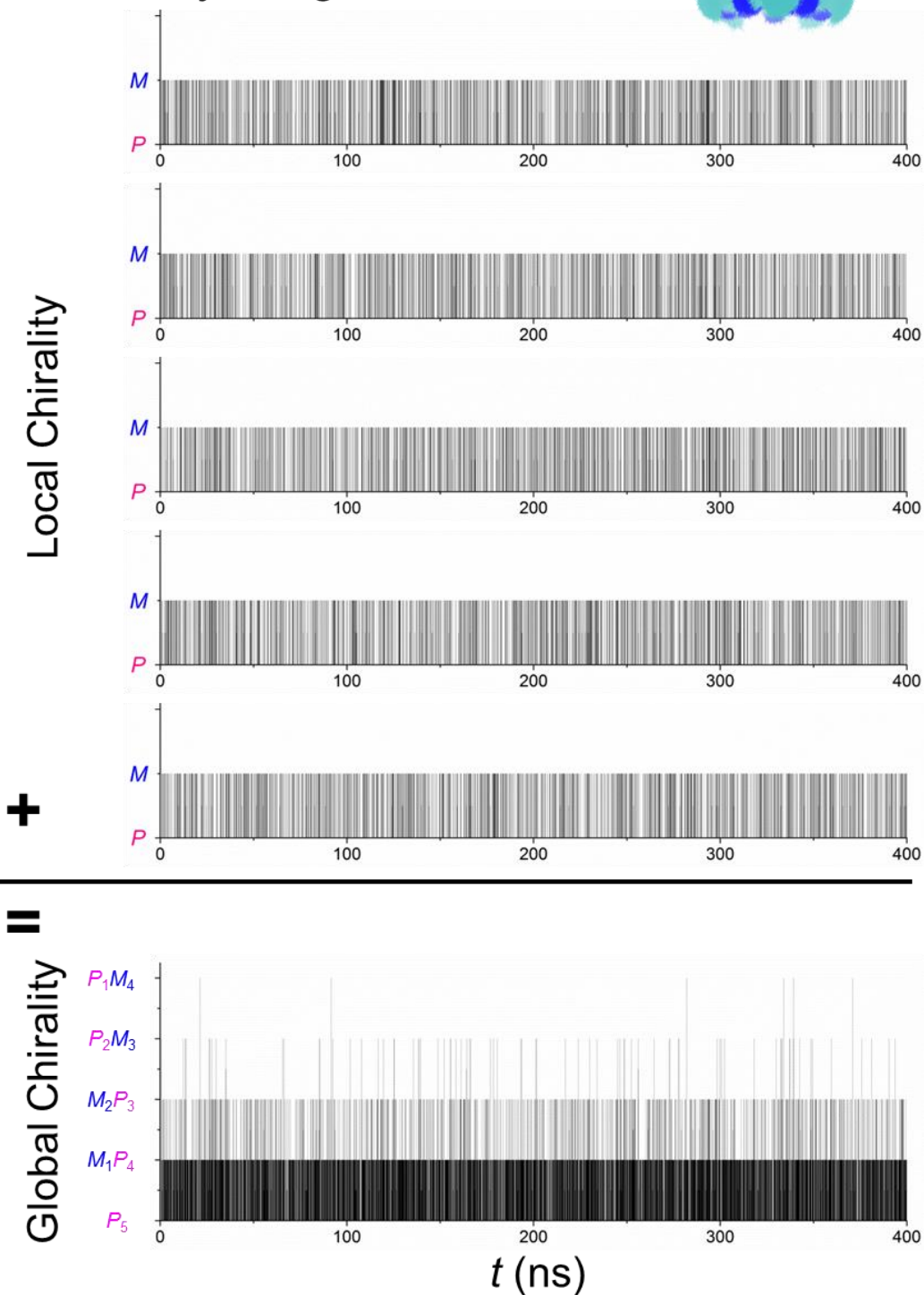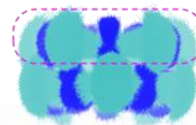
Figure S23. The trajectories of the local chirality assignments for five olefins and their sum to the global chirality assignments for the *P* cyanostar macrocycle in the 2:1 *M-P* cyanostar-diglyme complex during the MD simulation (400 ns, 298 K).

The thermodynamics of olefin rotations were analyzed by free energy surfaces computed from probability mass functions[S8] on the distributions of dihedral angles with a bin size of 5° (Figure S24, Table S18).
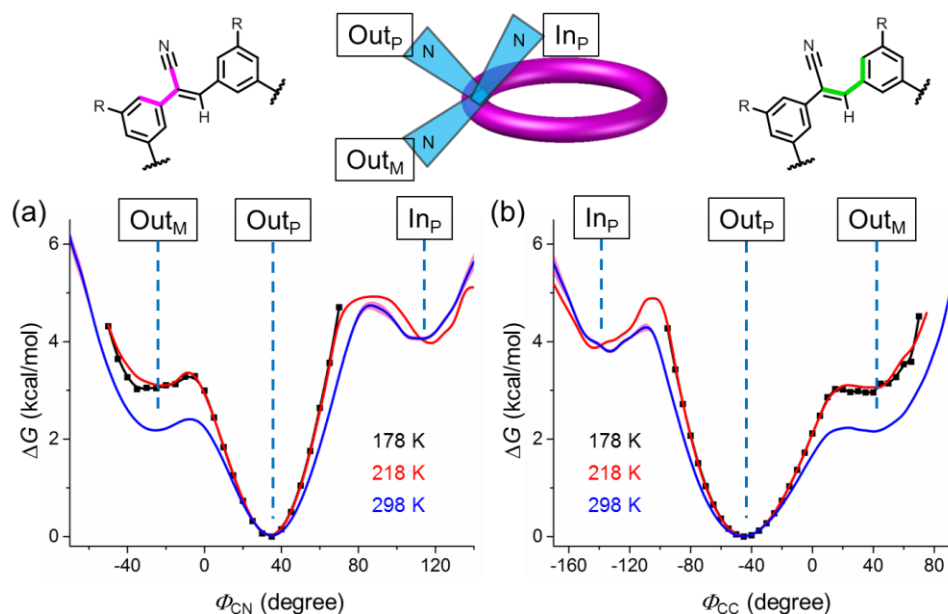
Figure S24. The free energy surfaces for olefin rotations using (a) Φ_{CN} and (b) Φ_{CC} at various temperatures. For clarity, errors are only shown as pink areas for the 298 K data.

S.7.2 Diglyme Binding to Cyanostar Dimers

Intermolecular displacements, R, between the center of the diglyme ($\bar{x}$, $\bar{y}$, $\bar{z}$) and the center of a M-P cyanostar dimer ($\bar{x}'$, $\bar{y}'$, $\bar{z}'$) in Å were collected every 2 ps. The relative stability was further analyzed by free energy surfaces (Figure S25), which were computed from probability mass functions[S8] with a bin size of 0.1 Å (Figure S26).
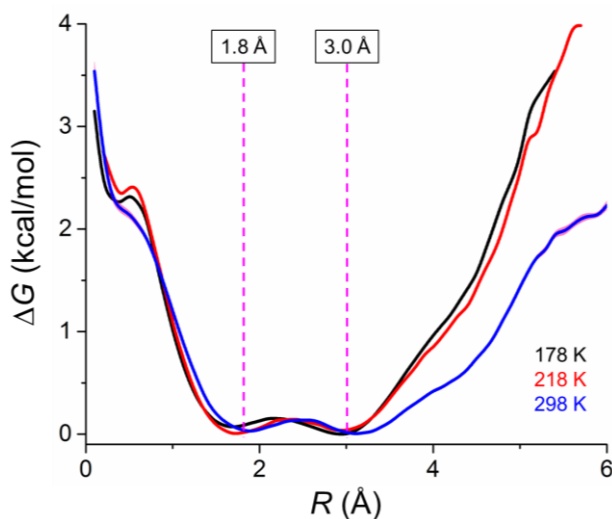
Figure S25. The free energy surfaces for diglyme debinding using intermolecular displacements, R, at various temperatures. For clarity, errors are only shown as pink areas for the 298 K data.
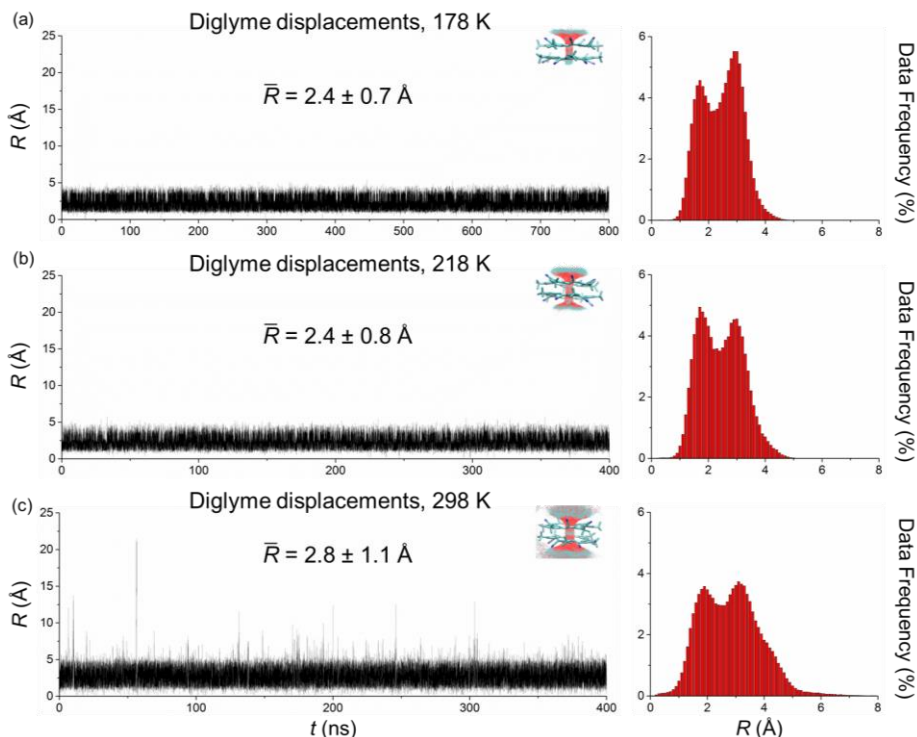
Figure S26. The trajectories of intermolecular displacements, R, between diglyme and an *M-P* cyanostar dimer during MD simulations and their corresponding equilibrium distributions at (a) 178 K, 800 ns; (b) 218 K, 400 ns; (c) 298 K, 400 ns.

S.7.3 Impact of Hydrogen Bonding to Changing Landscape of 2:1 Complexes

The same analysis was performed on the *M-P* 2:1 cyanostar-diglyme complexes. The protocol was modified from section **S.6.3** to address one difference that the bowl inversion of cyanostar in a sandwich complex is considered as a hypothetical equilibrum that start from a new global minima: P_5 for *P* conformers and M_5 for *M* conformers. Thus, the new conformer identity, Σ, can be derived directly from global chirality, Σ_{global}:

$$\text{Local chirality: } L = [-\text{Sign}(\Phi_{\text{CN}} - \Phi_{\text{CC}}) + 1] \times 0.5$$

$$\text{Global chirality: } \Sigma_{\text{global}} = \sum L_i \ (n = 5, i = 1)$$

$$\text{Conformer identity: } \Sigma = \text{Sign} (\Sigma_{\text{global}})$$

The Σ_{global} term will provide the following values for isomers: $P_5 = 0$, $P_4M_1 = 1$, $o\text{-}P_3M_2 = 2$, $m\text{-}P_3M_2 = 2$, $o\text{-}P_2M_3 = 3$, $m\text{-}P_2M_3 = 3$, $P_1M_4 = 4$, $M_5 = 5$. Therefore, any frame that has any *M* local chirality will be labelled by a positive integer. Overall, when conformers other than P_5 occur in the simulation of *P* conformers, the corresponding frame will be labelled with a value of **1**.

The same ratio, α, was defined and the results under different boundaries and temperatures are summarized in Table S19. In most cases, the value of α is close to 1, indicating

that hydrogen bonding between the hosts and the guest are playing a very minor role to the change in landscape. However, if the same equilibrium constants are calculated for the monomer case by assuming P_5 and M_5 are the global minima, the changes in both empty and complexed are over two orders of magnitudes. For instance, the K_{iso}(Free) calculated for single, free cyanostars are ~19.

Table S19. Cooperativity (α) between local chirality changes and diglyme debinding from a *P-M* 2:1 diglyme-cyanostar complex.

T(K)	R_0 (Å)[a]	K_{iso}(Free)	K_{iso}(Dig)	α
178	3	0.002	0.0017	1.2
218	3	0.008	0.006	1.3
	3	0.20	0.17	1.2
298	6	0.20	0.18	1.1
	9	0.43	0.18	2.4

S.7.4 Diglyme Binding to *Meso* and Homo-*chiral* Cyanostar Dimers

The binding between the diglyme molecule and the two diastereomers of the cyanostar dimers, i.e., *meso* (*M-P*) and homo-*chiral* (*P-P*), are compared. The intermolecular displacements of diglyme to *M-P* or *P-P* dimers were collected from two separate MD simulations, each of which was performed for 500 ns. Free energy surfaces (Figure S27) were computed from the probability mass functions[S8] with a bin size of 0.1 Å. The relative low stability associated with diglyme binding to *P-P* dimers is evident: (a) shallower free energy surfaces at regions where diglymes begin to escape from the dimer cavity ($R > 4$ Å); (b) the 3.1-Å minima is slightly more populated than the 1.9-Å minima; (c) the average displacement for diglymes is larger with *P-P* dimers as hosts; (d) wider distribution and thus lower data frequency for *P-P* dimer with any chosen bin size (Figures S28 and S29).
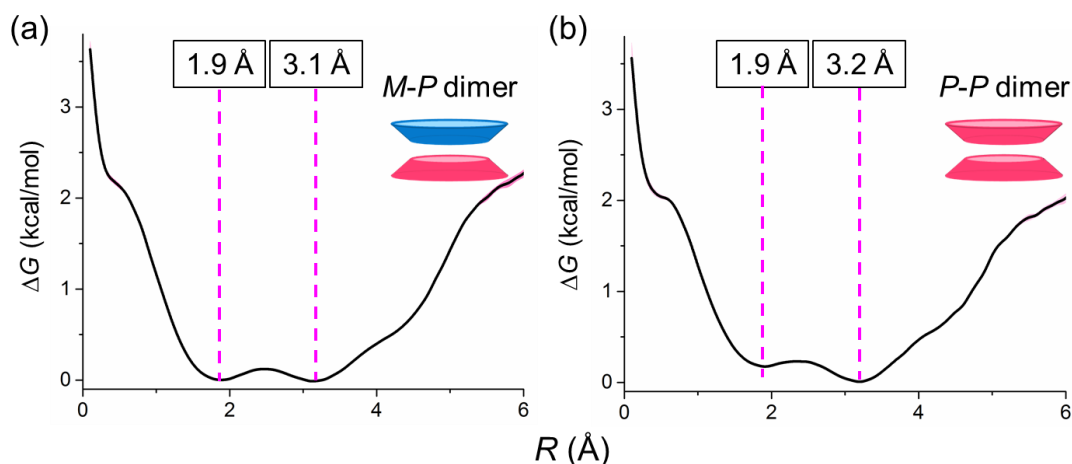
Figure S27. The free energy surfaces for diglyme debinding with (a) *M-P* dimer and (b) *P-P* dimer using intermolecular displacements, *R*, at 298 K. Errors are shown as pink areas.
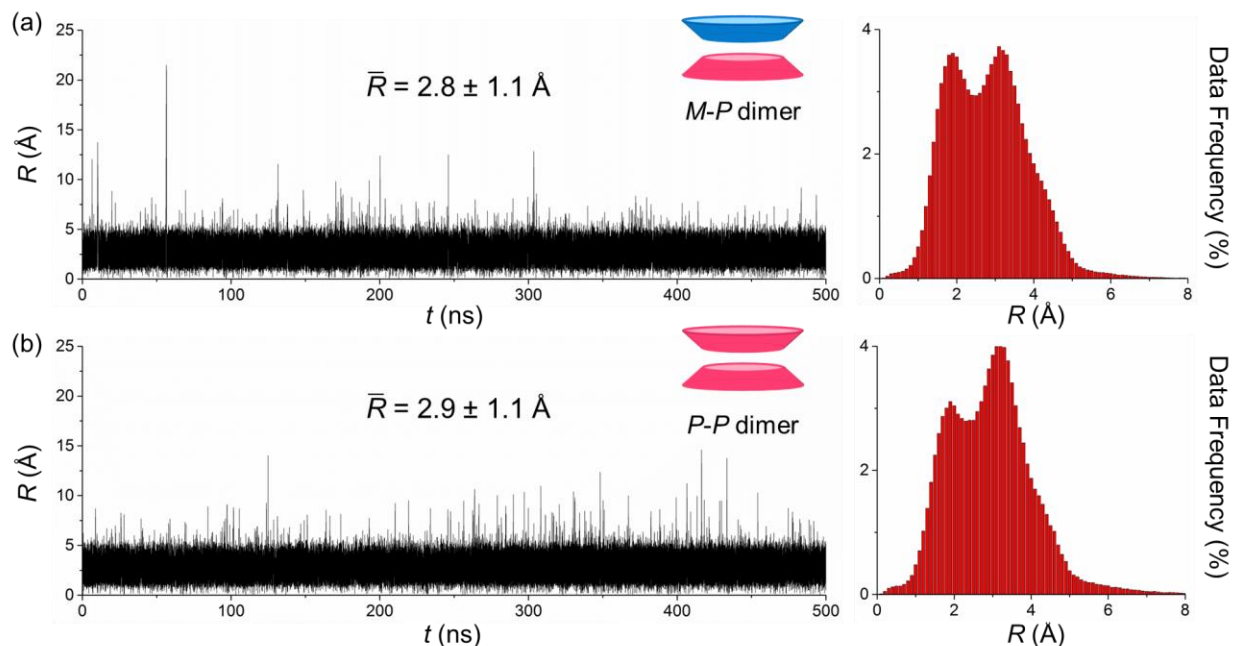
Figure S28. The trajectories of intermolecular displacements, *R*, between diglyme and (a) an *M-P* dimer and (d) a *P-P* dimer, and their corresponding equilibrium distributions during MD simulations (500 ns, 298 K).
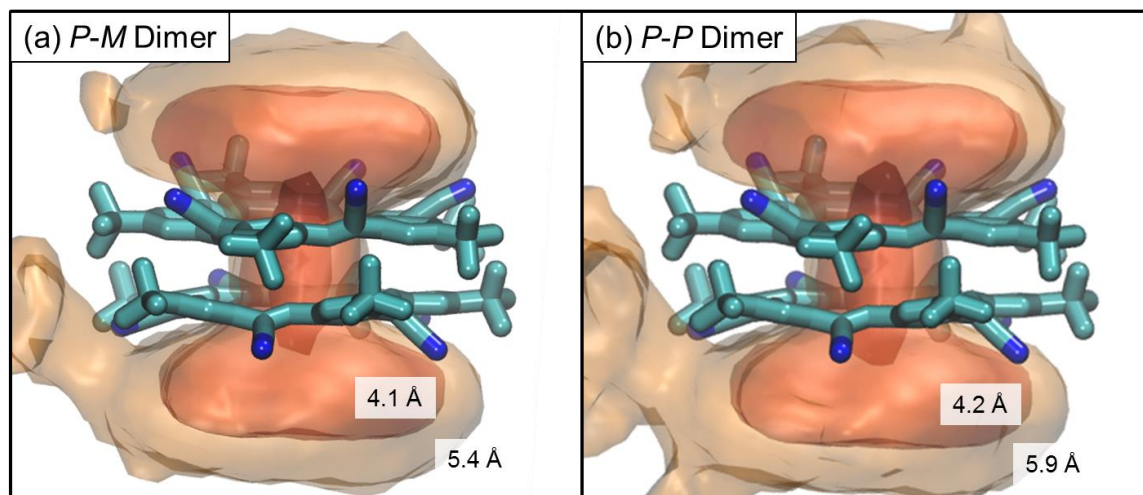
Figure S29. Occupancy maps of diglyme inside (a) a *meso* dimer and (d) a *homo*-chiral dimer. Three isodensity surfaces were shown indicating a 50, 90, and 99% chance of finding diglyme within them. The center-to-center displacements (*R*) associated with the 90 and 99% isosurfaces are shown; the colors of the surface indicate the density on the surface, with red for high density.

S.8 Dynamic Stability of Bowl Chirality Inversions

Correlation coefficient, *C*, represents the ensemble-average ordering, or dynamic stability, for a structural property between its initial distribution and the distribution after certain period of lag time, τ. The normalized coefficient ranges between 1 and −1; a positive coefficient indicates a

positive correlation, and *vice versa*. By changing the lag time, the lifetime correlation functions, $C(\tau)$, reveal the τ-dependent evolution of correlation coefficients: how fast and to what degree does the structural property loses dynamic stability and relax. Depending on the nature of the structural property studied and the normalization scheme, the coefficient does not always relax to the value of 0.

S.8.1 Lifetime Correlation Functions using Dihedral Angles

The dynamic stability of olefin rotations was investigated in two ways: self-ordering and relative ordering between neighbours. To evaluate self-ordering, auto-correlation coefficients,[9] C_{ii}, were calculated for the dihedral angles (Φ_i) of the five olefins ($i = 1$ to 5):

$$C_{ii}(\Phi, \tau) = \langle \Phi_i(t) \cdot \Phi_i(t + \tau) \rangle / \langle \Phi_i(t) \cdot \Phi_i(t) \rangle$$

where τ is the sampling interval, with a value of 2 ps to be consistent with the sampling interval used in the MD simulations. Finally, the reported time correlation functions were averaged over 10 traces ($5\Phi_{CN} + 5\Phi_{CC}$, Figure S30).
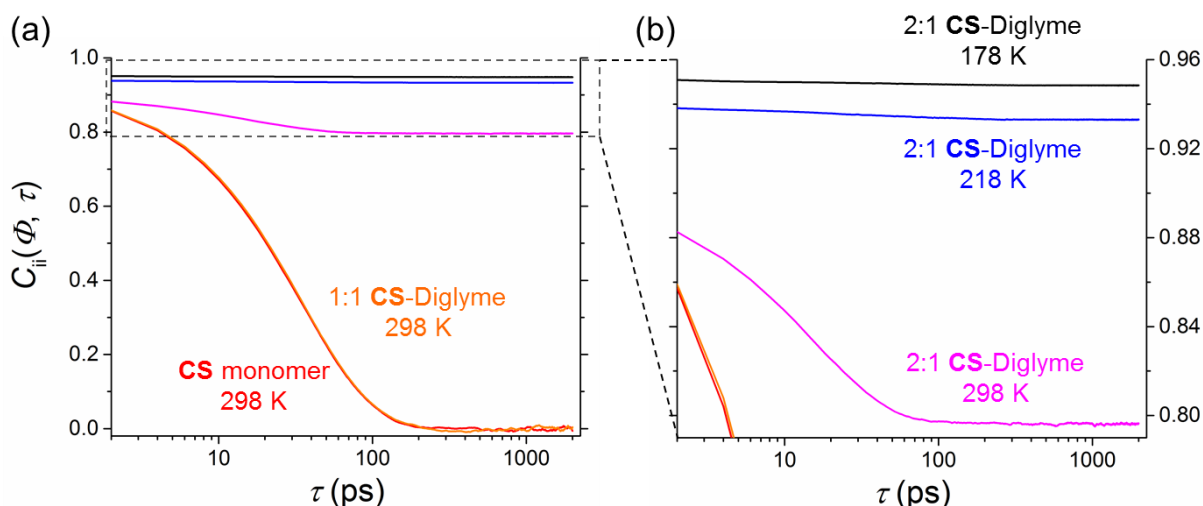
Figure S30. (a) The time autocorrelation functions based on dihedral angles and (b) a zoomed-in view for 2:1 cyanostar-diglyme complexes at various temperatures.

To characterize the relaxation processes for the coherent ordering of olefin rotations, the lifetime autocorrelation functions were baseline-corrected and fitted to a multi-exponential decay (Figure S31), where A_i is the fluctuation magnitude, τ_i^* is the relaxation time constant:

$$C_{ii}(\tau) = \sum A_i \cdot exp\left(-\tau / \tau_i^*\right)$$

We found that in most cases, a double exponential decay describes best the overall relaxations; single exponential usually cannot fit fast relaxations (< 20 ps) properly, while triple exponential yields the same fitting quality as double exponentials (Table S20). On account of the fact that there is negligible decay at low temperature for 2:1 complexes, the result of analysis was shown for data collected at 298 K.
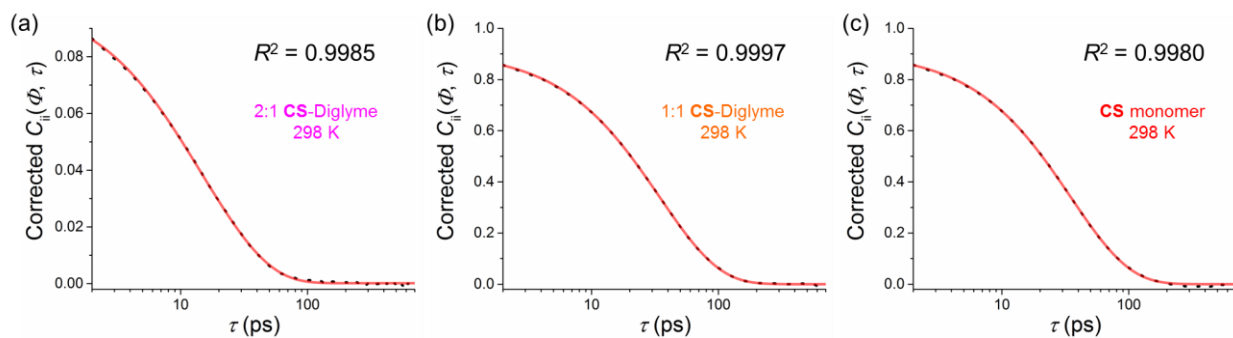
Figure S31. Fitting of relaxation time constants for the time autocorrelation functions of (a) the 2:1 cyanostar-diglyme complex, (b) the 1:1 cyanostar-diglyme complex, and (c) the cyanostar monomer at 298 K. The raw data are shown as black dotted lines, fitted curves are shown with red solid lines.

Cross-correlation coefficients (C_{ij}, i, j = 1 to 5; Figure S32) were calculated for olefins that are ortho ($|i - j| = 1$) or meta ($|i - j| = 2$) to each other:

$$C_{ij}(\Phi, \tau) = <\Phi_i(t) \bullet \Phi_j(t + \tau)> / <\Phi_i(t) \bullet \Phi_i(t)>$$

Ortho-positioned dihedral angles within single cyanostars show anti-correlation ($C_{ij} < 0$) to each other. This indicates that dipole-dipole interaction favors the cyano groups to be in the opposite side of the macrocyclic plane.

Table S20. Relaxation time constants for the time autocorrelation functions of olefin rotations in cyanostar macrocycles at 298 K.

Condition	τ_1 (ps)	τ_2 (ps)	Baseline[a]
2:1 complex	6 ± 1	20 ± 1	0.796
1:1 complex	14 ± 1	39 ± 1	0
Free cyanostar	15 ± 5	39 ± 1	0.002

[a]Baselines were obtained by averaging data beyond 1000 ps.
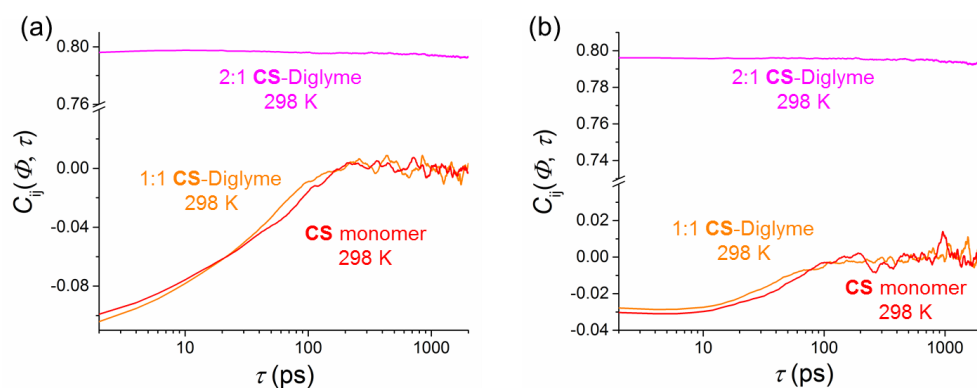
Figure S32. The time cross-correlation functions based on dihedral angles for (a) the 1,2-positioned and (b) the 1,3-pisitioned olefins.

S.8.2 Lifetime Correlation Functions using Local Chirality

The dynamic stability of local chirality (L_i, $i = 1$ to 5) for the five olefin units are evaluated. Auto-correlation coefficients (C_{ii}, $i = 1$ to 5; Figure S33) and cross-correlation coefficients (C_{ij}, i, $j = 1$ to 5; Figure S35) were calculated (section **S.8.1**):

$$C_{ii}(L', \tau) = <L'_i(t) \bullet L'_i(t + \tau)> / <L'_i(t) \bullet L'_i(t)>$$

$$\text{Or } C_{ij}(L', \tau) = <L'_i(t) \bullet L'_j(t + \tau)> / <L'_i(t) \bullet L'_i(t)>, \text{ where } i \neq j$$

where $L' = -L + 1$. When calculating correlation using the local chiral identity (L), the majority of the data has a value of 0 for macrocycle with P chirality in the 2:1 complexes. Analysis on these datasets returned zero correlation on account of the fact that the numerical outcome is zero. To avoid using a zero-dominated dataset, the distributions were reversed to have M chirality digitized as 0 for all cases during the calculation of correlation coefficients.
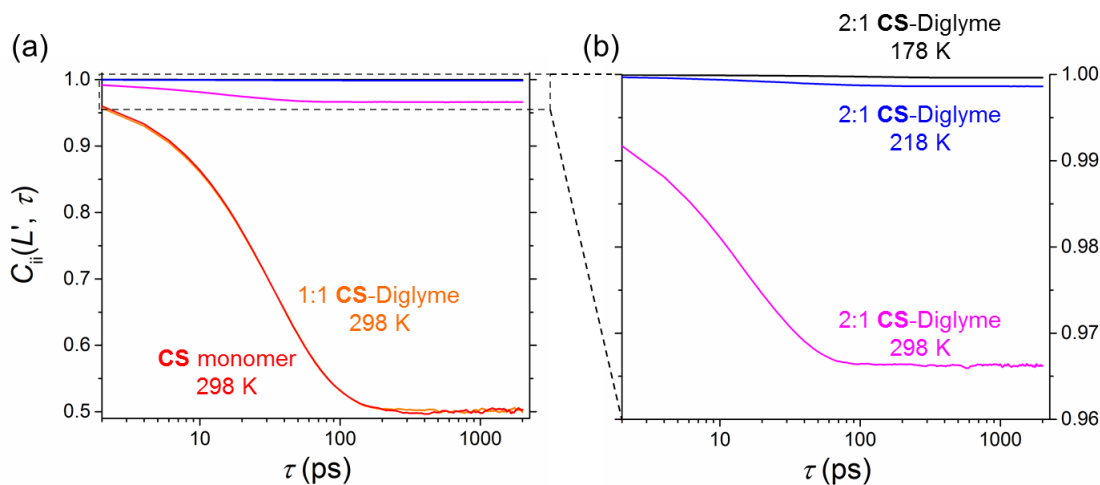
Figure S33. (a) The time autocorrelation functions based on local chirality identities and (b) a zoomed-in view for the 2:1 cyanostar-diglyme complex.

The chirality-based time autocorrelation functions were baseline-corrected and fitted to the same formula of multi-exponential decay (Figure S34):

$$C_{ii}(\tau) = \sum A_i \bullet exp\,(-\tau / \tau_i^*)$$

The relaxation based on local chirality has a simpler composition compared to those based on dihedral angles. We found in most cases even a single exponential decay can fully describe the whole relaxation process (Table S21).

By using local chirality, the correlation for the 2:1 complex showed a much simpler picture – a "permanent" chiral memory over time: both C_{ii} and C_{ij} were around 1, indicating almost full retention of the original chirality. For the 1:1 complex and free cyanostar, the C_{ii} and C_{ij} approached 0.5 over time. On the basis that a value of 1 for the autocorrelation coefficient suggests full retention of the original chirality, a value of 0 will indicate a complete chirality

inversion. Thus, the observation that $C_{ii}(L'_i, \tau)$ asymptotically approached 0.5, a perfect mixture of 0 and 1, suggests that the local chirality of olefins evolved into a state where there exists an equal population of M and P chirality (section **S.8.2.1**). For cross-correlations of olefin units within the monomer and the 1:1 complex, the coefficients (C_{ij}) started with a value of 0.48 and then approached 0.5. We then showed in the following section (section **S.8.2.2**) that the value of C_{ij} in these cases can be obtained from equilibrium statistics.
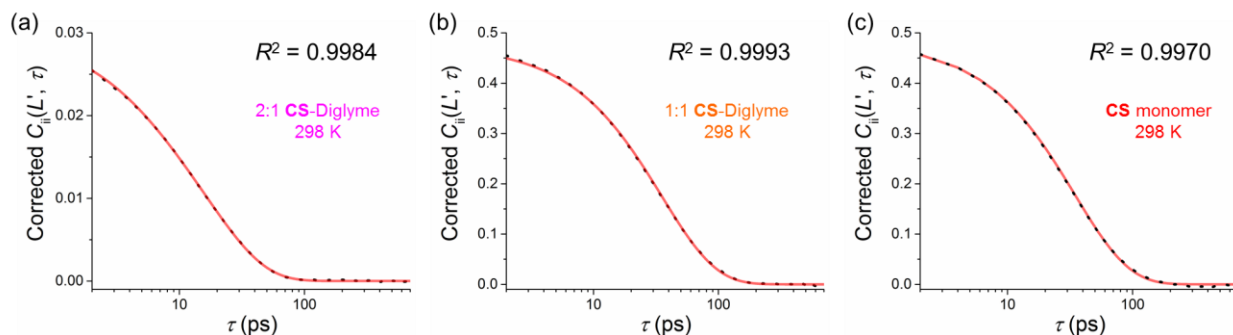
Figure S34. Fitting of relaxation times for the autocorrelation functions of (a) the 2:1 cyanostar-diglyme complex, (b) the 1:1 cyanostar-diglyme complex, and (c) the cyanostar monomer at 298 K. The raw data are shown as black dotted lines, fitted curves are shown with red solid lines.

Table S21. Relaxation time constants for the time autocorrelation functions of olefin rotations in cyanostar macrocycles at 298 K.

Condition	τ_1(ps)	τ_2 (ps)	Baseline[a]
2:1 complex [b]	4 ± 1	18 ± 1	0.966
1:1 complex	35 ± 1^c	–	0.502
Free cyanostar	35 ± 1^c	–	0.502

[a]Baselines were obtained by averaging data beyond 1000 ps. [b]The weighted-average relaxation time is 16 ps. [c]Double exponentials did not improve fitting quality, indicative of negligible second components.
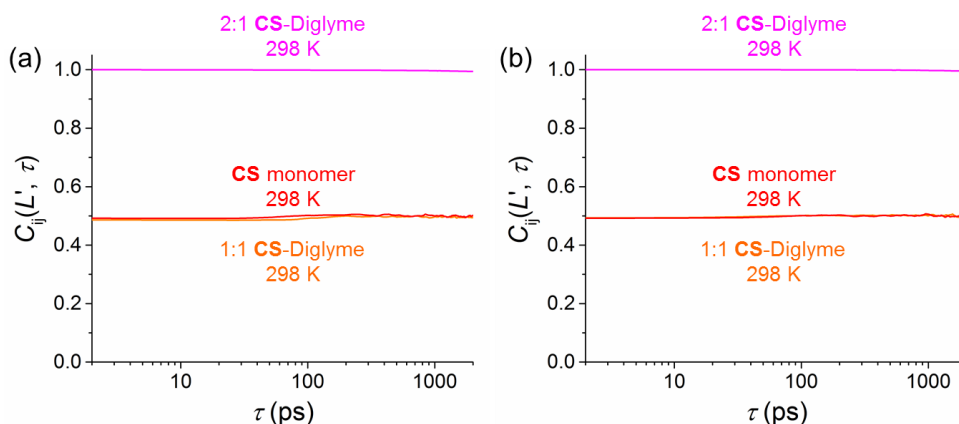
Figure S35. The time cross-correlation functions based on local chirality of (a) the 1,2-positioned olefins and (b) the 1,3-positioned olefins at 298 K.

S.8.2.1 Auto-correlation for Single Cyanostars with Long Lag Time. The autocorrelation coefficients (C_{ii}) with no lag time are essentially 2nd raw moments of the investigated distribution.[S9] To calculate the 2nd raw moments of the distribution of local chirality, $<L'_i(t) \bullet L'_i(t)>$, the probability mass function, $p_{ii}[L'_i(t) \rightarrow L'_i(t)]$, was used:

$$<L'_i(t) \bullet L'_i(t)> = \sum L'_i(t)^2 \bullet p_{ii}[L'_i(t) \rightarrow L'_i(t)]$$

The probability to express P and M chirality are identical and time-invariant for cyanostar monomers at equilibrium, $p_i(P) = p_i(M) = 0.5$. With no delay, all data certainly remain its original values; that is to say, the situation of P chirality remaining as P has the same probability as finding olefins to be in P chirality, and *vice versa*. Thus,

$$p_{ii}[L'_i(t) \rightarrow L'_i(t)] = p_{ii}(P \rightarrow P) = p_i(P) = p_i(M) = p_{ii}(M \rightarrow M) = 0.5.$$

Using these values along with the modified values for local chirality, $L'(P) = 1$, $L'(M) = 0$, autocorrelation coefficients with no delay, $<L'_i(t) \bullet L'_i(t)>$, can be calculated:

$$\sum L'_i(t)^2 \bullet p(L' \bullet L') = L'_i(P, t)^2 \bullet p_{ii}(P \rightarrow P) + L'_i(M, t)^2 \bullet p_{ii}(M \rightarrow M)$$

$$= (1 \times 1 \times 0.5) + (0 \times 0 \times 0.5) = 0.5$$

When the local chirality is allowed to develop over time, the equilibrium distribution will be completely statistical. Olefins develop from P chirality forward to M and back with equal probability (detailed balance). The probability mass function will then be:

$$p_{ii}[L'_i(t) \rightarrow L'_i(t + \tau)] = p_{ii}(P \rightarrow P) = p_{ii}(P \rightarrow M) = p_{ii}(M \rightarrow P) = p_{ii}(M \rightarrow M) = 0.25$$

Thus, with a very large lag time, the autocorrelation coefficient, $<L'_i(t) \bullet L'_i(t + \tau)>$, can be calculated:

$$<L'_i(t) \bullet L'_i(t + \tau)> = \sum L'_i(t) \bullet L'_i(t + \tau) \bullet p_{ii}[L'_i(t) \rightarrow L'_i(t + \tau)]$$

$$= L'_i(P, t) \bullet L'_i(P, t + \tau) \bullet p_{ii}(P \rightarrow P) + L'_i(P, t) \bullet L'_i(M, t + \tau) \bullet p_{ii}(P \rightarrow M)$$

$$+ L'_i(M, t) \bullet L'_i(P, t + \tau) \bullet p_{ii}(M \rightarrow P) + L'_i(M, t) \bullet L'_i(M, t + \tau) \bullet p_{ii}(M \rightarrow M)$$

$$= (1 \times 1 \times 0.25) + (1 \times 0 \times 0.25) + (0 \times 1 \times 0.25) + (0 \times 0 \times 0.25)$$

$$= 0.25$$

To normalize the autocorrelation coefficient with a very large lag time, $<L'_i(t) \bullet L'_i(t + \tau)>$, to the autocorrelation coefficient with no delay, $<L'_i(t) \bullet L'_i(t)>$:

$$C_{ii}(L', \tau) = <L'_i(t) \bullet L'_i(t + \tau)> / <L'_i(t) \bullet L'_i(t)> = 0.25 / 0.5 = 0.5$$

This derivation showcases that over time an olefin will eventually spend equal amount of time as P and M. Thus, the time autocorrelation function, $C_{ii}(L', \tau)$, represents how the olefin

unit starts with any one type of chirality and then evolves into a state where there exists an equal population of P and M.

S.8.2.2 Cross-correlation for Single Cyanostars with No Lag Time. To investigate the time cross-correlation function at no delay time, the derivation based on equilibrium statistics (section **S.8.2.1**) can be applied here by using the probability mass function, $p_{ij}[L'_i (t) \to L'_i (t) \mid L'_j (t) \to L'_j (t)]$, or $p_{ij}[L'_i (t) \mid L'_j (t)]$ since there is no delay time and no evolution:

$$\langle L'_i(t) \bullet L'_j(t) \rangle = \sum L'_i(t) \bullet L'_j(t) \bullet p_{ij}[L'_i (t) \mid L'_j (t)]$$

For cyanostar monomers at equilibrium, there are four pairs of enantiomers: P_5 and M_5 (L_5), P_4M_1 and M_4P_1 ($L_4L^{-1}_1$), $o\text{-}P_3M_2$ and $o\text{-}M_3P_2$ ($o\text{-}L_3L^{-1}_2$), and $m\text{-}P_3M_2$ and $m\text{-}M_3P_2$ ($m\text{-}L_3L^{-1}_2$), where L^{-1} indicates the opposite chirality to whichever L originally refers to. To simplify the calculation, we exploit situations that will return non-zero coefficients, i.e., cases where both local chirality have the value of 1:

$$L'_i(t) = L'_j(t) = 1$$

Under current definition of local chirality, $L'(P) = 1$, the raw moments can be calculated by exploiting the probability to find both olefins of interest, either 1,2-positioned (showcased in this section) or 1,3-positioned, in P chirality. This rationale allows the probability to be decomposed into two components. **First**, the probability of finding a certain stereoisomer at the equilibrium, e.g., $p(L_5)$ is the relative population of P_5 and M_5 at equilibrium. **Second**, the probability to have neighboring olefins with P chirality for that certain stereoisomer, $p_{ij}[P \mid P]$, which is invariant for a certain stereoisomers. Using the L_5 cyanostar as an example, all five 1,2-neighbouring olefin units are present in P chirality in a P_5 isomer while none of the five present in P in an M_5 isomer, $p_{ij}[P \mid P; L_5] = 5/10 = 0.5$. To repeat this procedure for all stereoisomers:

$$\sum L'_i(t) \bullet L'_j(t) \bullet p_{ij}(L'_iL'_j) = L'_i(P, t) \bullet L'_j(P, t) \bullet p(L_5) \bullet p_{ij}[P \mid P; L_5]$$

$$+ L'_i(P, t) \bullet L'_j(P, t) \bullet p(L_4L^{-1}_1) \bullet p_{ij}[P \mid P; L_4L^{-1}_1]$$

$$+ L'_i(P, t) \bullet L'_j(P, t) \bullet p(o\text{-}L_3L^{-1}_2) \bullet p_{ij}[P \mid P; o\text{-}L_3L^{-1}_2]$$

$$+ L'_i(P, t) \bullet L'_j(P, t) \bullet p(m\text{-}L_3L^{-1}_2) \bullet p_{ij}[P \mid P; m\text{-}L_3L^{-1}_2]$$

$$= 0.5 \bullet p(L_5) + 0.3 \bullet p(L_4L^{-1}_1) + 0.3 \bullet p(o\text{-}L_3L^{-1}_2) + 0.1 \bullet p(m\text{-}L_3L^{-1}_2)$$

Based on the MD simulation, the above summation to the cross-correlation coefficient at no delay, $\langle L'_i(t) \bullet L'_j(t) \rangle$, is 0.24. To normalize this cross-correlation coefficient:

$$C_{ij}(L', t) = \langle L'_i(t) \bullet L'_j(t) \rangle / \langle L'_i(t) \bullet L'_i(t) \rangle = 0.24 / 0.5 = 0.48$$

Overall, the equilibrium-statistics-based derivation reproduces the cross-correlation coefficients for local chirality of olefin units present at 1,2-positions. Over time, individual olefin units eventually lose their memory of their original chirality and enter a state of coexisting, equal

population of *P* and *M*. Thus, the cross-correlation coefficients behave the same as autocorrelation coefficient with a very large lag time.

S.9 Planarity of Single Cyanostars

S.9.1 Planarity Based on MD simulations

An MD simulation was performed for a single cyanostar macrocycle at 298 K using an implicit dichloromethane solvent medium (ε_r = 8.9). The simulations were performed for 540 ns and structural parameters were collected every 2 ps. The structural parameters collected were proton-proton distances that are characteristic in NOE (*n*uclear *O*verhauser *e*ffect) experiment (Figure S36). There are in total 10 traces of distances for protons that are inside the cavity, H^c and H^d; there are 5 traces for distances between H^a and H^c.

Both proton pairs are within the distance range that allows for significant development of homonuclear NOE. In order to compare results obtained from MD simulation to those obtained from NOE experiment, proton-proton distances were averaged in the form of $1/r^6$:

$$\langle r_{cd} \rangle_{MD} = [(\textstyle\sum_{i=1}^{F} \sum_{i=1}^{5} r_{cd}^{-6}) / 5F]^{-1/6}, \quad \langle r_{ac} \rangle_{MD} = [(\textstyle\sum_{i=1}^{F} \sum_{i=1}^{10} r_{ac}^{-6}) / 10F]^{-1/6}$$

Where *F* is the number of frames collected during the MD simulations. The average is done over the 5 repeating olefin units in the cyanostar molecule as well as all frames within one unit collected during the MD simulation. In an NOE experiment for cyanostar, the distance ratio, *n*, between these two distances is used in the comparison:

$$n_{MD} = \langle r_{ac} \rangle_{MD} / \langle r_{cd} \rangle_{MD} = 1.63 \pm 0.12$$
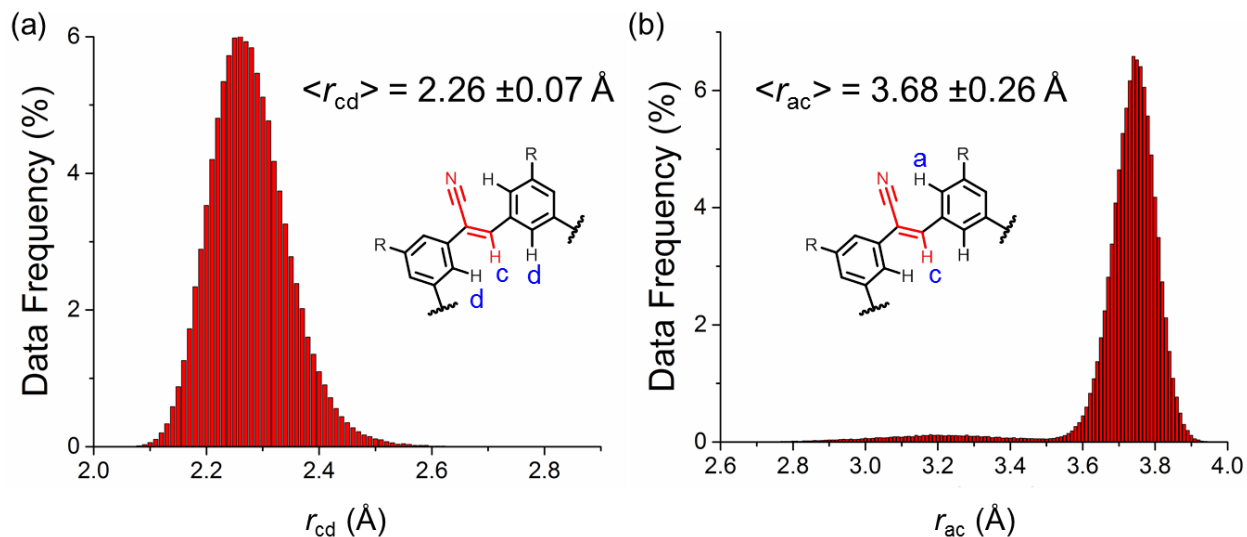
Figure S36. The equilibrium distribution and the average proton-proton distances for (a) H^c-H^d and (b) H^a-H^c pairs.

S.9.2 Planarity Based on Quantitative ^{1}H-^{1}H NOE Spectroscopy

The 2D ^{1}H-^{1}H NOESY (***n**uclear **O**verhauser **e**ffect **s**pectroscop**y*) was performed on a 500 MHz Varian Inova spectrometer to measure the relative proton-proton distances in cyanostar at 298 K (Figure S37). 10 mM CD_2Cl_2 solution of cyanostar was used. The 90° ^{1}H pulse was calibrated to be 11.6 μs. The T_1 relaxation times were measured for all protons and the longest T_1 for the aromatic protons was found to be 2.6 s. The delay time was then set to $3T_1$ of 8.4 s. A wide range of mixing time, t_{mix} = 25 to 600 ms, was explored. Mixing times that are shorter than 200 ms were insufficient to yield measureable NOE signals, and the data are not used in the fitting. The 2D spectra were collected by the same set of parameters: number of transients (nt = 4) for the f_2 dimension, number of increments (ni = 128) for the f_1 dimension. The spectra were processed by the same window function: Gaussian window function was used on both f_1 (gf_1 = 0.5*ni/sw_1, 32.98 Hz) and f_2 dimensions ($gf = at/2$, 8.28 Hz).
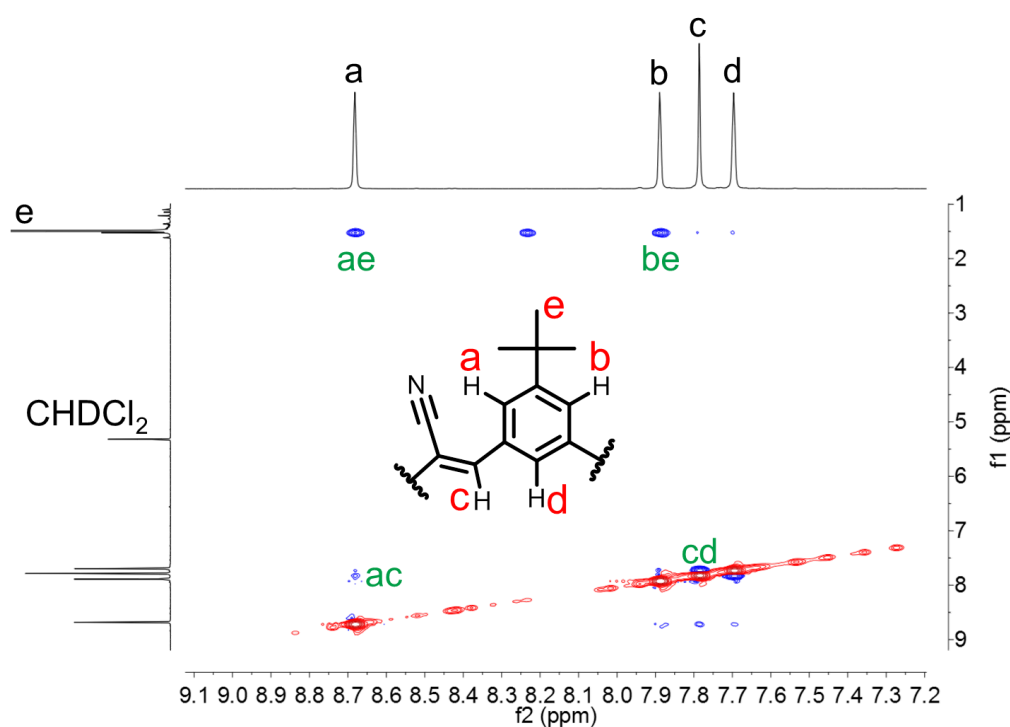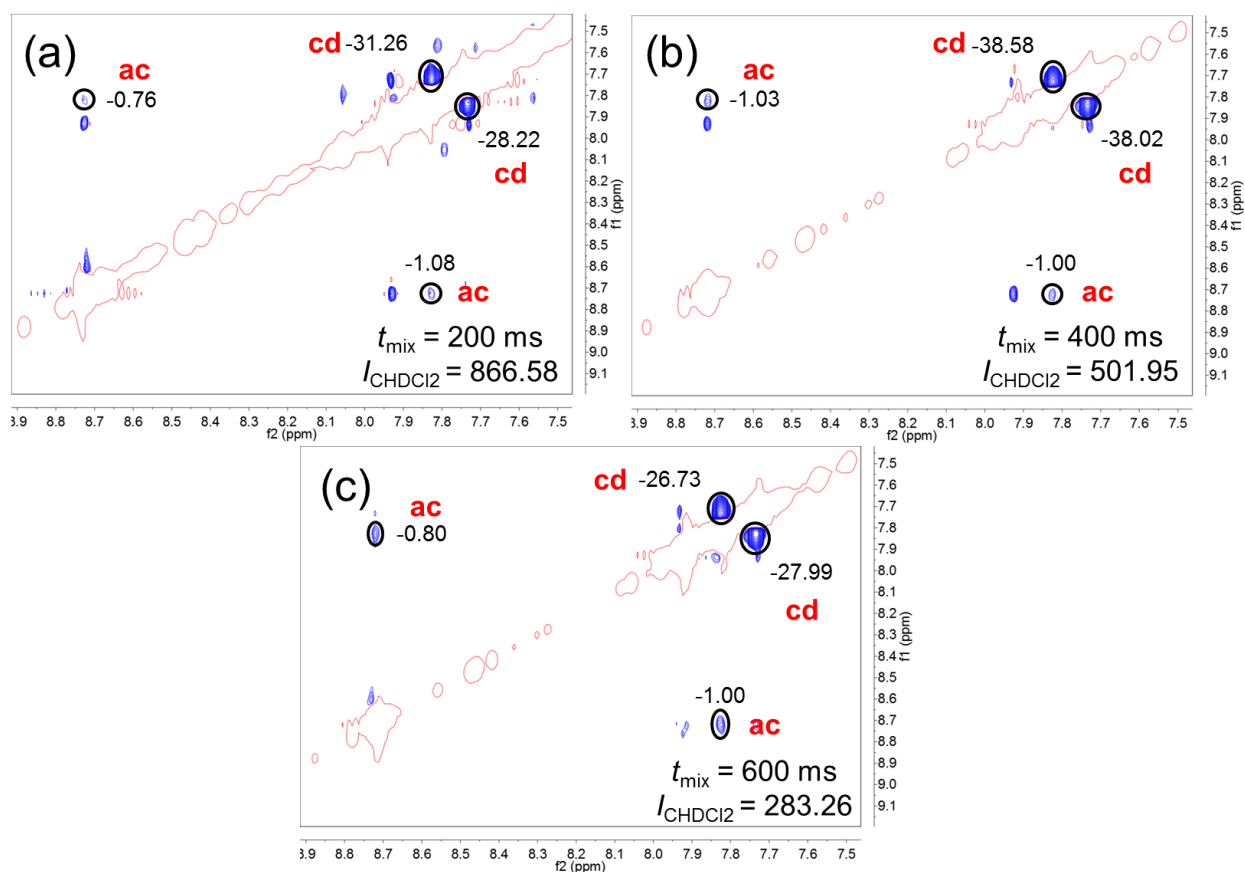

Figure S37. ^{1}H-^{1}H NOE spectrum of cyanostar (10 mM, CD_2Cl_2, 500 MHz, 298 K).

The 2D integrations of cross-correlation peaks from different spectra were measured in software MestReNova and normalized using the solvent diagonal signal (Figure S38). To overcome potentially imperfect baseline, both off-diagonal NOE correlations were combined and used in the fitting. Linear equation with no intercept was used to obtain the slope, k, which is the NOE build-up rate (Figure S39). Under the condition of short mixing time, the NOE build-up rate is proportional to $<N/r^6>$, where r is the proton-proton distances, and N is the number of the corresponding correlations (N_{cd} = 10, N_{ac} = 5):[S10]

$$k_{cd}/k_{ac} = (N_{cd}/N_{ac}) \bullet (<r_{cd}>_{NOE}/<r_{ac}>_{NOE})^{-1/6}$$

So, $n_{NOE} = <r_{ac}>_{NOE}/<r_{cd}>_{NOE} = 1.60 \pm 0.01$

Figure S38. Aromatic region of ^{1}H-^{1}H NOE spectra (500 MHz, 298K) of cyanostar with increasing mixing time: (a) 200 ms, (b) 400 ms, and (c) 600 ms. The integrations (I_{CHDCl2}) of corresponding solvent diagonal peaks are noted.
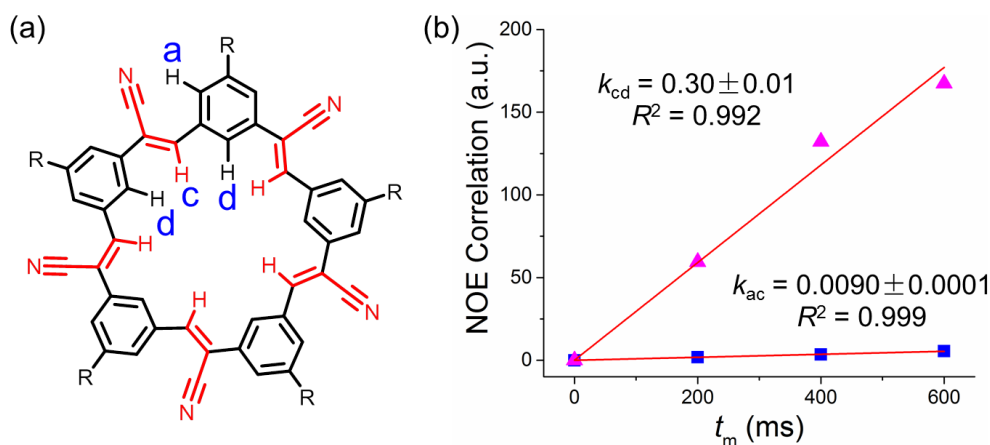
Figure S39. (a) Labels for aromatic protons in the cyanostar macrocycle. (b) Linear data fitting for the NOE correlations for H^a-H^c (blue squares) and H^c-H^d (magenta triangles) proton pairs.

S.9.3 Planarity Based on DFT calculations

Based on the optimized geometries from section **S.1**, proton-proton distances can be measured on all conformers and then averaged using their population ($p_{soln,i}$, Table S1):

$$<r_{cd}>_{DFT} = [(\sum_{i=1}^{34} \sum_{i=1}^{5} r_{cd}^{-6} \cdot p_{soln, i}) / 5]^{-1/6}, <r_{ac}>_{DFT} = [(\sum_{i=1}^{34} \sum_{i=1}^{10} r_{ac}^{-6} \cdot p_{soln, i}) / 10]^{-1/6}$$

Where the summation is performed over two levels: 5 or 10 pairs of proton-proton distances within one conformation and 34 conformations. The distance ratios are listed for all conformers and compared to the other two methods (Table S22).

*Table S22.* Proton-proton distances within cyanostar conformers.

Isomers	$<r_{cd}>$ (Å)	$<r_{ac}>$ (Å)	n_{DFT}	Isomers	$<r_{cd}>$ (Å)	$<r_{ac}>$ (Å)	n_{DFT}
P_5	2.15	3.80	1.77	$o\text{-}M_2P_3\text{-}5$	2.28	3.17	1.39
M_1P_4	2.19	3.81	1.74	$o\text{-}M_2P_3\text{-}1,3$	2.34	2.93	1.25
$M_1P_4\text{-}1$	2.27	3.22	1.42	$o\text{-}M_2P_3\text{-}1,4$	2.33	2.92	1.25
$M_1P_4\text{-}2$	2.28	3.20	1.41	$o\text{-}M_2P_3\text{-}2,4$	2.32	2.90	1.25
$M_1P_4\text{-}3$	2.26	3.20	1.41	$o\text{-}M_2P_3\text{-}2,5$	2.33	2.92	1.25
$M_1P_4\text{-}4$	2.26	3.18	1.41	$o\text{-}M_2P_3\text{-}3,5$	2.34	2.93	1.25
$M_1P_4\text{-}5$	2.27	3.15	1.39	$m\text{-}M_2P_3$	2.20	3.86	1.76
$M_1P_4\text{-}1,3$	2.29	2.90	1.26	$m\text{-}M_2P_3\text{-}1$	2.25	3.22	1.43
$M_1P_4\text{-}1,4$	2.29	2.95	1.29	$m\text{-}M_2P_3\text{-}2$	2.30	3.21	1.40
$M_1P_4\text{-}2,4$	2.31	2.90	1.26	$m\text{-}M_2P_3\text{-}3$	2.30	3.23	1.41
$M_1P_4\text{-}2,5$	2.30	2.91	1.27	$m\text{-}M_2P_3\text{-}4$	2.30	3.23	1.40
$M_1P_4\text{-}3,5$	2.31	2.73	1.18	$m\text{-}M_2P_3\text{-}5$	2.26	3.22	1.42
$o\text{-}M_2P_3$	2.21	3.81	1.73	$m\text{-}M_2P_3\text{-}1,3$	2.33	2.91	1.25
$o\text{-}M_2P_3\text{-}1$	2.28	3.20	1.40	$m\text{-}M_2P_3\text{-}1,4$	2.35	2.96	1.26
$o\text{-}M_2P_3\text{-}2$	2.29	3.19	1.40	$m\text{-}M_2P_3\text{-}2,4$	2.34	2.92	1.25
$o\text{-}M_2P_3\text{-}3$	2.29	3.20	1.40	$m\text{-}M_2P_3\text{-}2,5$	2.34	2.92	1.25
$o\text{-}M_2P_3\text{-}4$	2.27	3.19	1.40	$m\text{-}M_2P_3\text{-}3,5$	2.34	2.68	1.14

$n_{DFT} = 1.57$; $n_{MD} = 1.63$; $n_{NOE} = 1.60$.

S.10 ^{1}H NMR Titration of Cyanostar with Diglyme

The titration of cyanostar with diglyme was monitored by ^{1}H NMR spectroscopy at room temperature (298 K) on a 500 MHz Varian Inova spectrometer. 600 μL of 10 mM host solutions were prepared in screw-cap NMR tubes equipped with PTFE/silicone septa. Aliquots of pure liquid diglyme (1.1 eq / μL) in screw-cap vials equipped with PTFE/silicone septa were added using a 100 μL gas-tight micro-syringe. The binding constant β was then fitted to a 2:1 model ($CS_2 \cdot$ Diglyme) by HypNMR 2009 using proton H^a to H^d from cyanostar (Figure S40). The

β was fitted to be ~30 M^{-2} with reasonably good quality, $\sigma = 4.8$. The binding was very weak in solution phase, thus excess amount of diglyme was required to generate meaningful dataset for fitting. However, the solvent composition was slightly modified at the very end of the titration to 1:4 v/v diglyme:dichloromethane. Although the molar ratio was small (10%) for diglyme at the end of the titration and the dielectric environment was not significantly altered, $\varepsilon_r(CH_2Cl_2) = 8.9$ vs ε_r (diglyme) $= 7.3$, this binding constant will only be used for qualitative comparison.
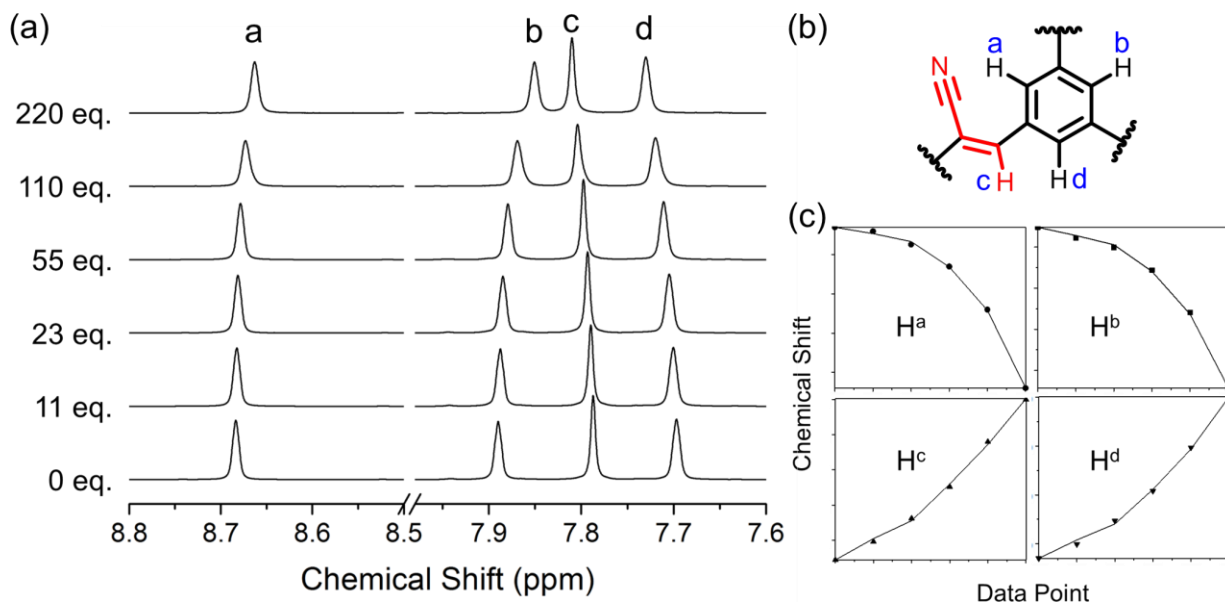
Figure S40. (a) ^{1}H NMR titration of cyanostar (10 mM) in CD$_2$Cl$_2$ with diglyme (equivalents as listed, 500 MHz, 298 K). (b) Proton labels of cyanostar. (c) Fitting curves for protons H^a to H^d.

S.11 Variable-Temperature ^{1}H NMR Spectra of Cyanostar

The variable temperature ^{1}H NMR spectroscopy of cyanostar was performed on a 500 MHz Varian Inova spectrometer. Cyanostar was prepared as a 10 mM CD$_2$Cl$_2$ solution.
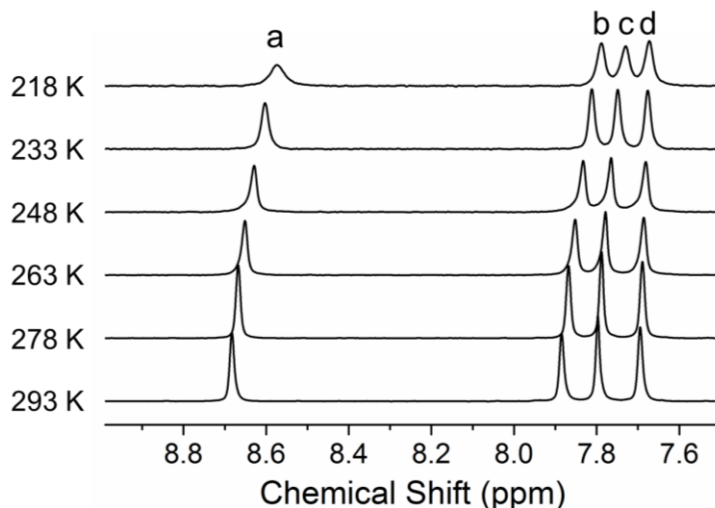
Figure S41. ^{1}H NMR spectra of cyanostar (10 mM) in CD$_2$Cl$_2$ at various temperatures.

References

S1 Frisch, M. J.; Trucks, G. W.; Schlegel, H. B.; Scuseria, G. E.; Robb, M. A.; Cheeseman, J. R.; Scalmani, G.; Barone, V.; Mennucci, B.; Petersson, G. A.; Nakatsuji, H.; Caricato, M.; Li, X.; Hratchian, H. P.; Izmaylov, A. F.; Bloino, J.; Zheng, G.; Sonnenberg, J. L.; Hada, M. ; Ehara, M.; Toyota, K.; Fukuda, R.; Hasegawa, J.; Ishida, M.; Nakajima, T.; Honda, Y.; Kitao, O.; Nakai, H.; Vreven, T.; Montgomery Jr., J. A.; Peralta, J. E.; Ogliaro, F.; Bearpark, M. J.; Heyd, J.; Brothers, E. N.; Kudin, K. N.; Staroverov, V. N.; Kobayashi, R.; Normand, J.; Raghavachari, K.; Rendell, A. P.; Burant, J. C.; Iyengar, S. S.; Tomasi, J.; Cossi, M.; Rega, N.; Millam, N. J.; Klene, M.; Knox, J. E.; Cross, J. B.; Bakken, V.; Adamo, C.; Jaramillo, J.; Gomperts, R.; Stratmann, R. E.; Yazyev, O.; Austin, A. J.; Cammi, R.; Pomelli, C.; Ochterski, J. W.; Martin, R. L.; Morokuma, K.; Zakrzewski, V. G.; Voth, G. A.; Salvador, P.; Dannenberg, J. J.; Dapprich, S.; Daniels, A. D.; Farkas, O.; Foresman, J. B.; Ortiz, J. V.; Cioslowski, J. ; Fox, D. J. *Gaussian 09*, Gaussian, Inc., Wallingford, CT, USA, 2009.

S2 Zhao, Y.; Truhlar, D. G. *Theor. Chem. Acc.* **2008**, *120*, 215–241.

S3 Miertus, S.; Scrocco. E.; Tomasi, J. *Chem. Phys.* **1981**, *55,* 117–129.

S4 Grimme, S. *Chem. Eur. J.* **2012**, 18, 9955–9964.

S5 Szumna, A. *Chem. Soc. Rev.* **2010**, *39*, 4274–4285.

S6 Phillips, J. C.; Braun, R.; Wang, W.; Gumbart, J.; Tajkhorshid, E.; Villa, E.; Chipot, C.; Skeel, R. D.; Kale, L.; Schulten, K. *J. Comput. Chem.* **2005**, *26*, 1781–1802.

S7 Singharoy, A.; Venkatakrishnan, B.; Liu, Y.; Mayne, C. G.; Lee, S.; Chen, C.-H.; Zlotnick, A.; Schulten, K.; Flood, A. H. *J. Am. Chem. Soc.* **2015**, *137*, 8810–8818.

S8 Based on Boltzmann statistics, the probability mass function can be calculated: $p_i = N_i/\Sigma N_i$. N_i is the number of events categorized in each bin (i).

S9 Pathria, R. K.; Beale, P. D. *Statistical Mechanics*, 3rd ed.; Academic Press Waltham: 2011.

S10 Jacobsen, N. E. *NMR Spectroscopy Explained: Simplified Theory, Applications and Examples for Organic Chemistry and Structural Biology*, 1st ed.; Wiley: New York, 2007.